Development of a V-Band 2-Path (2SQCC) Continuous Calibrating Spectrometer based on the Multi Path Cross Correlation Radiometry (MXCR) Technique

by

Aravind Venkitasubramony

B.Tech., University of Kerala, 2006

M.Eng., University of Michigan, 2013

A thesis submitted to the
Faculty of the Graduate School of the
University of Colorado in partial fulfillment
of the requirement for the degree of
Doctor of Philosophy
Electrical and Computer Engineering
2025

Committee Members:

Albin Gasiewski, Chair

Taylor Barton

Cody Scarborough

Gregor Lasser

Nicole Bienert

Venkitasubramony, Aravind (Ph.D., Electrical and Computer Engineering)
Development of a V-Band 2-Path (2SQCC) Continuous Calibrating Spectrometer based on the Multi Path Cross Correlation Radiometry (MXCR) Technique

Thesis directed by Prof. Albin Gasiewski

This thesis discusses the work done towards the design, development and field testing of the first ever 2-path V-band 2SQCC digital correlating spectrometer based on the Multipath Cross Correlation Radiometry (MXCR) concept. The theoretical background and mathematical analysis of an ideal and practical 2SQCC transmission network architecture is presented. The implementation challenges encountered in instrument development and design recommendations towards the development of future instruments based on the MXCR concept are discussed. A technique to measure and compensate for the effects of cross-talk in the cross-correlation estimate between two receiver paths in the MXCR scheme is developed and implemented. The clear sky brightness temperature spectra from 51-54 GHz measured using the 2SQCC spectrometer is compared with the microwave radiative transfer model prediction. The observed spectrum is found to be matching the prediction within a few kelvins of offset attributable to the usage of an average atmospheric model. The work done towards the integration of the 2SQCC spectrometer to a spectrum broker orchestrating co-operative spectrum sharing between active and passive services is discussed.

ACKNOWLEDGEMENTS

NASA Earth and Space Sciences Fellowship (Award: 80NSSC17K0324)

NSF Collaborative research SWIFT Spectrum Innovation Initiative Award: 2030243

Texas Instruments Inc. for generous hardware and software support.

Weatherstream (Orbital Micro Systems) for VNA facilities

Mr. David Kraft, Lab manager (CU CET) for mechanical engineering assistance.

Prof. John Cressler and Dr. Milad Frounchi (Georgia Tech)

All present and past CET graduate and undergraduate students.

CONTENTS

LIST OF FIGURES

Figure

LIST OF TABLES

Table

CHAPTER 1

INTRODUCTION

1.1 Scientific Background & Motivation

The Paris climate agreements [1] were established with the goal of limiting the globally-averaged greenhouse warming of the atmosphere to "…well below 2 degrees Celsius above pre-industrial levels and to pursue efforts to limit the temperature increase even further to 1.5°C." Using the turn of the 21st century as the time horizon for these increases to have become manifested provides a benchmark for the relevant trends that need to be detected to unambiguously corroborate bulk atmospheric temperature changes with those established by the prevailing means of surface temperature measurements. These turn-of-century trends are thus 1.5°C/80 years (or 0.19°C/decade) in an ideal scenario and up to ~3.5°C/80 years or more (i.e., greater than 0.43°C/decade) in the more serious of warming scenarios. To be able to quantify the anticipated future trends on a timely (~decadal) basis the globally-averaged mid-tropospheric temperature thus needs to be observed with a satellite temperature sounding instrument of drift of less than 0.061°C/decade, both diurnally and globally. This precision is required to be able to detect the lowest of the above anticipated trends with 99% (i.e., 6-sigma) confidence. Given nominal spacecraft lifetimes of ~7 years, there is thus a requirement for ~0.061/√2=0.043K RMS combined sounder stability and repeatability between successive instruments for the lowest of these warming trends to be observed at the 6-sigma level of confidence.

Satellite temperature measurements are essential for monitoring global atmospheric temperature changes, distinguishing human-induced climate signals from natural variability [2], and assessing numerical General Circulation Models

(GCMs). Instruments like the Microwave Sounding Unit (MSU), Advanced Microwave Sounding Unit (AMSU), and Advanced Technology Microwave Sounder (ATMS) have been used since 1978 to create temperature trend records for the lower troposphere and lower stratosphere, albeit indirectly. These instruments originally designed for weather forecasting purposes do not have the high stability, precision, and traceability needed for climate studies, leading to temperature records with variabilities that complicate the accurate assessment of climatological temperatures [3]. These variabilities are caused by calibration and local oscillator (LO) drifts, instrument non-linearity, changes in local measurement times (diurnal cycle shifts), and uncertainties related to the channel spectral characteristics. Additionally, these instruments were created in an era with minimal anthropogenic radio frequency interference (RFI), which is expected to become more prevalent in future climate missions.

The past 50-years temperature trends have been measured primarily through surface-based measurements [4] and are of the order of 0.16°C/decade. Relying solely on surface measurements for model validation poses the risk of systematic biases in the temperature trends due to heat-island effects caused by urbanization [5,6] and differences between boundary layer and bulk atmospheric temperature [7].

Radiometer gain and offset instability is known to introduce scan "striping error" during a long scan exceeding ~0.3 K in some ATMS channels [8]. The Cosmic Background Explorer (COBE) and Wilkinson Microwave Anisotropy Probe (WMAP) [9] missions using a differential pseudo-correlation architecture were able to achieve very high stability, but these missions observed continuum background radiation with little spectral variation, while all conventional temperature sounders (including ATMS) observe within discrete channels within the lower wing of the 5-mm O2 band of up to ~400 MHz bandwidth. This relatively large bandwidth results in up to several kelvin of sub-channel spectral variation that is an additional source of inter-sensor

calibration error. Such large intra-channel variation warrants that a sounder used for either climate reference or intercalibration purposes be able to spectrally resolve all relevant tropospheric and stratospheric emission features.

Another source of uncertainty in temperature records arises from the change in spectral passband response between the generations of satellite sensors [10]. The channels used for tropospheric measurements (MSU channel 2 and AMSU channel 5) differ significantly, as do the channels used for lower stratospheric measurements (MSU channel 4 and AMSU channel 9). The last MSU instrument on NOAA-14 satellite and the early AMSU instruments operated at different local times, intercalibrating these instruments is challenging without more precise knowledge of the diurnal cycle at each frequency. Stable and traceable measurements with high spectral resolution, would (1) enhance adjustments for diurnal non-climatic artifacts in existing satellite records and (2) establish a standardized method for measuring future temperature records.

With the advances in cubesat technologies and cheaper access to space, several commercial satellite sounding missions are also on in operation now compared to a couple of decades ago. At any given time, several satellites with temperature-sounding instruments are in orbit, but each has a finite lifetime. The multiplicity of sounders will increase significantly with the anticipated deployment of commercial sounding constellations [11-13]. Therefore, intercalibration of these instruments is increasingly necessary to produce reliable Climate Data Records (CDRs) of temperature and stabilize numerical weather prediction model forecasts using these data. Goldberg et al. [14] [15] point out a need for on-orbit reference instruments with high stability and traceability, without which instrumental drift or deterioration might obscure trends occurring over several decades.

Accordingly, there is a compelling need to observe across the entire ~8,000 MHz of the 5-mm O2 band from 50-58 GHz with ~1 MHz spectral resolution. Use of this wide band is further warranted to achieve high radiometric sensitivity, for surface temperature correction, and to measure temperature variations over the entire tropospheric and stratospheric column (Figure 1.1).

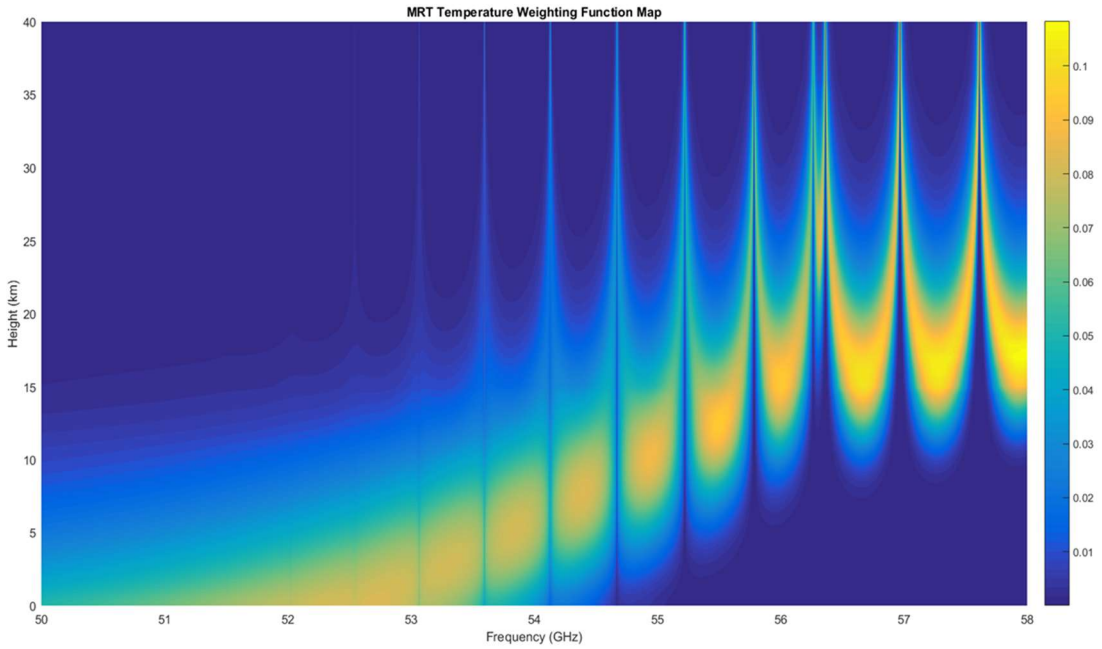

Figure 1.1 Clear-air temperature weighting function spectra (in km^{-1}) for the lower wing of the 5mm oxygen temperature sounding band from 50-58 GHz. Calculations used the Microwave Radiative Transfer (MRT) model [16], a dry US standard atmosphere [17] profile and the MPM87 attenuation model [18].

We are entering an era of increased anthropogenic emission resulting from the imminent deployment of fifth generation (5G) communications electronics [19-20] and related consumer and defense applications at V-band which will be significantly different from the times the heritage instruments like MSU, AMSU, and ATMS were conceived and operated. The second harmonic emissions (if any) from the n257 band

(26.5-29.5 GHz), and n258 (24.25 – 27.5 GHz) band fall on the bandwidths of the current operational weather sounders which are not equipped with RFI detection capability [21]. Given the historical trend of spectral occupancy doubling every ~6 years, RFI detection and mitigation is critical to future imaging and sounding radiometer architectures.

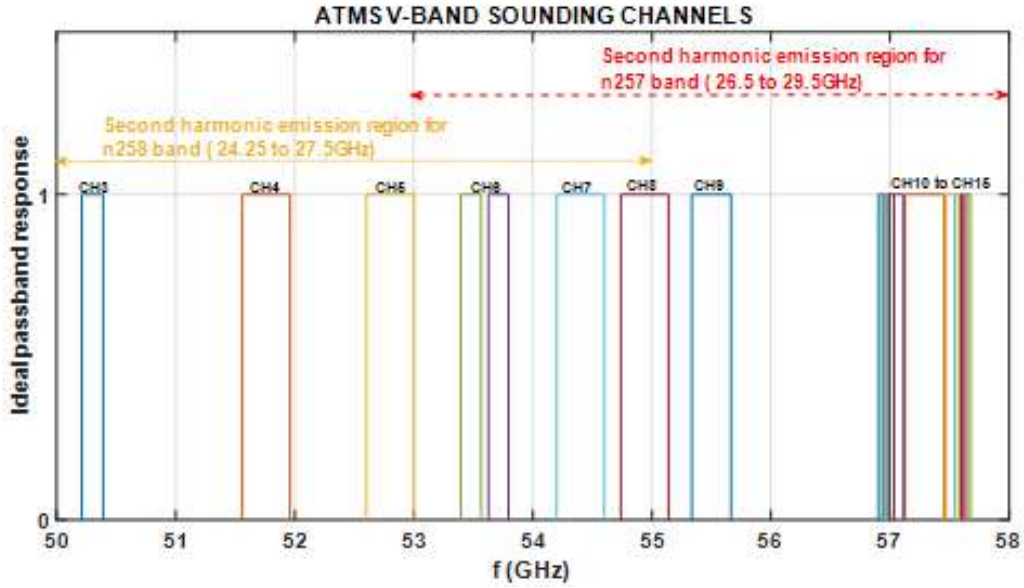

Figure 1.2. ATMS Sounding Channels (50-58 GHz) and second harmonic emission regions of 5G n257 and n258 bands.

This thesis details the work done towards the development of a stable high spectral resolution 2SQCC spectrometer based on a novel radiometer architecture, Multi Path Cross-correlating Radiometry (MXCR), to improve upon the challenges discussed above in the development of a climate reference instrument for atmospheric temperature sounding. The need and application of this instrument architecture in detecting, quantifying, and reporting RFI in a co-operative spectrum sharing paradigm is presented. The subsequent chapters discuss the concept, design, prototype development, laboratory and field testing of the 2SQCC spectrometer instrument.

CHAPTER 2

2SQCC TRANSMISSION NETWORK ANALYSIS

2.1 Multi Path Cross Correlation Radiometry (MXCR)

Traditional calibration of single-path and differential correlation radiometers relies on a series of measurements using precisely known internal or external temperature references. This process requires highly repeatable switching mechanisms and leads to a reduction in radiometric integration efficiency. The need for such calibration stems from the fact that the number of unknowns in the radiometer's response equation exceeds the number of measurements available at the detector.

A novel technique called **Multipath Cross-Correlation Radiometry (MXCR)** [22,23] addresses this limitation by utilizing cross-correlations of complex signals that are amplified and detected across multiple receiver paths. As the number of receiver paths (Np) exceeds three, the system becomes increasingly overdetermined, enabling a unique form of self-calibration that effectively neutralizes variations in path gain and phase. Alternatively, MXCR can use the system's many observational degrees of freedom to estimate these gain and phase values directly.

The method is particularly well-suited for cross-correlating digital spectrometers and provides exceptional robustness against gain saturation—whether caused by out-of-band radio frequency interference or low-frequency (1/f) internal gain fluctuation noise. This makes MXCR a powerful approach for stabilizing radiometers, radars, and communication receivers affected by gain modulation. Moreover, it enables high-precision radio frequency spectrometry that can be accurately calibrated against traceable physical temperature standards, even at frequencies reaching up to a terahertz or beyond.

In an MXCR receiver architecture, one unknown signal is mixed with multiple known signals in a passive combiner network to generate multiple output signals which are then independently amplified, digitally detected, and cross correlated. The passive combiner circuit in an MXCR architecture is called a “transmission network”. Depending on the number of independent output signal paths and the type of passive elements in the combiner network, different types of transmission networks can be realized.

2.2 Ideal 2SQCC Transmission Network

The minimum number of receiver paths needed in an MXCR scheme is two and there are different transmission network architectures that can be realized to validate this concept. The transmission network architecture realized here uses a combination of two couplers, one quadrature hybrid, and one sum-difference hybrid (Magic-T) and will be referred to as the “2SQCC” network from here on in this document. The 2SQCC transmission network architecture was chosen to leverage and repurpose WR19 hardware from previous projects. The nomenclature “2SQCC” is derived from the number of receiver paths and the type of passive devices used in the transmission network as follows.

2 – Number of paths
S – Sum-Difference Hybrid (Magic-T)
Q – Quadrature Hybrid
C – Cross guide coupler in path-01
C- Cross guide coupler in path-02

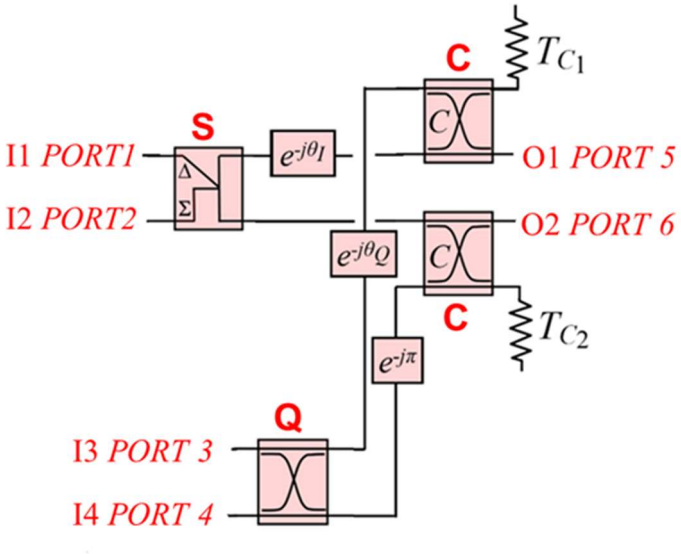

Figure 2.1 2SQCC Transmission Network Block Diagram

The 2SQCC front-end RF transmission network block diagram is given in Figure 2.1. There are four input ports labeled I1, I2, I3, and I4 and two output ports labeled O1, and O2. The path length difference between the two outputs of the Magic-T is modeled as $e^{-j\theta_I}$. The path length difference between the two outputs of the quadrature hybrid is modeled as $e^{-j\theta_Q}$. The handedness of the two cross-guide couplers needs to be opposite to each other to ensure a mechanical fit and is accounted for by the e^{-j} term in the block diagram. The two cross guide couplers are three port devices with internal terminations which are at temperatures denoted by T_{C1} and T_{C2}. The 2SQCC transmission network is thus a 6-port device.

The signal combining operation done by the 2SQCC transmission network can be represented mathematically using a 2 x 4 matrix $\bar{\bar{T}}$. The four input signals are combined in the transmission network generating two output signals. We will first consider the ideal transmission network where the two hybrids and the two cross guide couplers are assumed to be lossless. In this scenario, the transmission network $\bar{\bar{T}}$ can be written as follows in equation (2.1)

$$\bar{\bar{T}} = \frac{1}{\sqrt{2}} \begin{bmatrix} -j|C_{p_1}| & \sqrt{1-|C_{p_1}|^2} & 0 & 0 \\ 0 & 0 & \sqrt{1-|C_{p_2}|^2} & -j|C_{p_2}| \end{bmatrix} \begin{bmatrix} 0 & 0 & e^{-j\theta_Q} & 0 \\ e^{-j\theta_I} & 0 & 0 & 0 \\ 0 & 1 & 0 & 0 \\ 0 & 0 & 0 & e^{-j\pi} \end{bmatrix} \begin{bmatrix} 1 & 1 & 0 & 0 \\ -1 & 1 & 0 & 0 \\ 0 & 0 & 1 & -j \\ 0 & 0 & -j & 1 \end{bmatrix} \quad (2.1)$$

The transmission coefficients of the two cross guide couplers, sum-difference hybrid, and the quadrature hybrid are highlighted in the two blue boxes, red box, and green box respectively. The transmission network combines the brightness temperatures at the four input ports represented by the phasors $V_A, V_{R0}, V_{NR1}, and\ V_{NR2}$ to generate two output signals. The signal combining operation of the transmission network is represented as follows in equation (2.2)

$$\bar{\bar{T}} \begin{bmatrix} V_A \\ V_{Ro} \\ V_{NR_1} \\ V_{NR_2} \end{bmatrix} = \frac{1}{\sqrt{2}} \begin{bmatrix} V_A e^{-j\theta_I}\sqrt{1-|C_{p_1}|^2} - e^{-j\theta_Q}|C_{p_1}|V_{NR_2} - je^{-j\theta_Q}|C_{p_1}|V_{NR_1} + e^{-j\theta_I}\sqrt{1-|C_{p_1}|^2}\,V_{Ro} \\ \sqrt{1-|C_{p_2}|^2}\,V_{Ro} + |C_{p_2}|V_{NR_1} + j|C_{p_2}|V_{NR_2} - V_A\sqrt{1-|C_{p_2}|^2} \end{bmatrix} \quad (2.2)$$

The two signals generated by the transmission network combining operation are further amplified, coherently downconverted, band limited and sampled. The overall complex gains of the two amplifier chains are represented by $G_{v\pi 1}$ and $G_{v\pi 2}$ and the overall receiver noise power represented by the phasors V_{REC1} and V_{REC2}. C_1 and C_2 represent the complex FFT coefficients of the two individual path signal voltages. The block diagram of the 2SQCC spectrometer architecture is given in Figure 2.2.

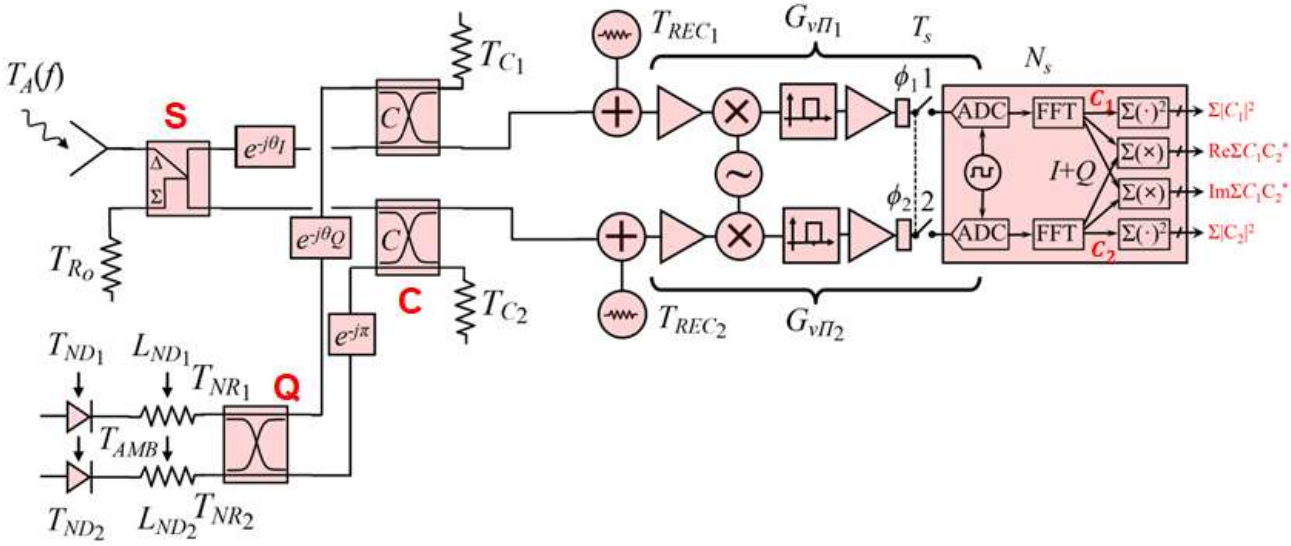

Figure 2.2 2SQCC Spectrometer Block Diagram

$$\begin{bmatrix} C_1 \\ C_2 \end{bmatrix} = \frac{1}{\sqrt{2}} \begin{bmatrix} G_{v\pi_1} & 0 \\ 0 & G_{v\pi_2} \end{bmatrix} \begin{bmatrix} V_A e^{-j\theta_I}\sqrt{1-|C_{p_1}|^2} - e^{-j\theta_Q}|C_{p_1}|V_{NR_2} - je^{-j\theta_Q}|C_{p_1}|V_{NR_1} + e^{-j\theta_I}\sqrt{1-|C_{p_1}|^2}\,V_{Ro} \\ \sqrt{1-|C_{p_2}|^2}\,V_{Ro} + |C_{p_2}|V_{NR_1} + j|C_{p_2}|V_{NR_2} - V_A\sqrt{1-|C_{p_2}|^2} \end{bmatrix} + \begin{bmatrix} \sqrt{2}\,V_{REC_1} \\ \sqrt{2}\,V_{REC_2} \end{bmatrix}$$

$$= \frac{1}{\sqrt{2}} \begin{bmatrix} G_{v\pi_1}\left(\sqrt{2}\,V_{REC_1} - je^{-j\theta_Q}|C_{p_1}|V_{NR_1} - e^{-j\theta_Q}|C_{p_1}|V_{NR_2} + V_A e^{-j\theta_I}\sqrt{1-|C_{p_1}|^2} + e^{-j\theta_I}\sqrt{1-|C_{p_1}|^2}\,V_{Ro}\right) \\ G_{v\pi_2}\left(\sqrt{1-|C_{p_2}|^2}\,V_{Ro} + |C_{p_2}|V_{NR_1} + j|C_{p_2}|V_{NR_2} - V_A\sqrt{1-|C_{p_2}|^2} + \sqrt{2}\,V_{REC_2}\right) \end{bmatrix} \tag{2.3}$$

The coherency matrix $\overline{\overline{J_C}}$ is a 2 x 2 matrix estimated for each FFT bin by multiplying the 2 x 1 FFT output vector with its Hermitian transpose.

$$\overline{\overline{J_c}} = \begin{bmatrix} C_1 \\ C_2 \end{bmatrix} \begin{bmatrix} C_1^* & C_2^* \end{bmatrix} = \begin{bmatrix} C_1C_1^* & C_1C_2^* \\ C_2C_1^* & C_2C_2^* \end{bmatrix} = \begin{bmatrix} c_{11} & c_{12} \\ c_{21} & c_{22} \end{bmatrix} \tag{2.4}$$

The individual elements of the coherency matrix are evaluated below. The diagonal terms c_{11} and c_{22} represent the total power in the two receiver paths.

$$c_{11} = \frac{1}{2}G_{\pi_1}^* G_{v\pi_1}\left(\sqrt{2}\,V_{REC_1} - je^{-j\theta_Q}|C_{p_1}|V_{NR_1} - e^{-j\theta_Q}|C_{p_1}|V_{NR_2} + V_A e^{-j\theta_I}\sqrt{1-|C_{p_1}|^2} + e^{-j\theta_I}\sqrt{1-|C_{p_1}|^2}\,V_{Ro}\right)$$
$$\left(\sqrt{2}\,V_{REC_1}^* + e^{j\theta_I}V_{Ro}^*\sqrt{1-|C_{p_1}|^2} + jV_{NR_1}^* e^{j\theta_Q}|C_{p_1}| - V_{NR_2}^* e^{j\theta_Q}|C_{p_1}| + e^{j\theta_I}V_A^*\sqrt{1-|C_{p_1}|^2}\right)$$

$$c_{22} = \frac{1}{2}G_{v\pi_2}^* G_{v\pi_2}\left(\sqrt{2}\,V_{REC_2}^* + V_{NR_1}^*|C_{p_2}| - jV_{NR_2}^*|C_{p_2}| - V_A^*\sqrt{1-|C_{p_2}|^2} + V_{Ro}^*\sqrt{1-|C_{p_2}|^2}\right) \tag{2.5}$$
$$\left(\sqrt{1-|C_{p_2}|^2}\,V_{Ro} + |C_{p_2}|V_{NR_1} + j|C_{p_2}|V_{NR_2} - V_A\sqrt{1-|C_{p_2}|^2} + \sqrt{2}\,V_{REC_2}\right)$$

The off-diagonal terms c_{21} and c_{12} are complex conjugates of each other and either one of the two off-diagonal terms can be used for retrieval using 2SQCC concept.

$$
\begin{aligned}
c_{21} = \tfrac{1}{2} G^*_{v\pi_1} G_{v\pi_2} \Big(& \sqrt{2}\, V^*_{REC_1} + e^{j\theta_I} V^*_{Ro} \sqrt{1-|C_{p_1}|^2} + jV^*_{NR_1} e^{j\theta_Q} |C_{p_1}| - V^*_{NR_2} e^{j\theta_Q} |C_{p_1}| + e^{j\theta_I} V^*_A \sqrt{1-|C_{p_1}|^2} \Big) \\
& \Big(\sqrt{1-|C_{p_2}|^2}\, V_{Ro} + |C_{p_2}| V_{NR_1} + j|C_{p_2}| V_{NR_2} - V_A \sqrt{1-|C_{p_2}|^2} + \sqrt{2}\, V_{REC_2} \Big)
\end{aligned}
\tag{2.6}
$$

$$
\begin{aligned}
c_{12} = \tfrac{1}{2} G^*_{v\pi_2} G_{v\pi_1} \Big(& \sqrt{2}\, V^*_{REC_2} + V^*_{NR_1} |C_{p_2}| - jV^*_{NR_2} |C_{p_2}| - V^*_A \sqrt{1-|C_{p_2}|^2} + V^*_{Ro} \sqrt{1-|C_{p_2}|^2} \Big) \\
& \Big(\sqrt{2}\, V_{REC_1} - je^{-j\theta_Q} |C_{p_1}| V_{NR_1} - e^{-j\theta_Q} |C_{p_1}| V_{NR_2} + V_A e^{-j\theta_I} \sqrt{1-|C_{p_1}|^2} + e^{-j\theta_I} \sqrt{1-|C_{p_1}|^2}\, V_{Ro} \Big)
\end{aligned}
$$

In evaluating the expressions for c_{11}, c_{22}, c_{21} and c_{12}, the following simplifications are used.

1. Multiplying a complex number with its complex conjugate is equivalent to squaring its magnitude and is a purely real number

$$
\begin{aligned}
G^*_{v\pi_1} G_{v\pi_1} &= |G_{v\pi_1}|^2 & \qquad G^*_{v\pi_2} G_{v\pi_2} &= |G_{v\pi_2}|^2 \\
V_{REC_1} V^*_{REC_1} &= |V_{REC_1}|^2 & \qquad V_{REC_2} V^*_{REC_2} &= |V_{REC_1}|^2 \\
V_A V^*_A &= |V_A|^2 & \qquad V_{Ro} V^*_{Ro} &= |V_{Ro}|^2 \\
V_{NR_1} V^*_{NR_1} &= |V_{NR_1}|^2 & \qquad V_{NR_2} V^*_{NR2} &= |V_{NR_2}|^2
\end{aligned}
\tag{2.7}
$$

2. Since the four input signals and the two receive noise voltages are all mutually uncorrelated, the expected value of the product pairs of any of these phasors will be zero.

$$
\begin{array}{lllll}
\langle V_{REC1} V^*_{NR1} \rangle = 0 & \langle V_{REC1} V^*_{NR2} \rangle = 0 & \langle V_{REC1} V^*_A \rangle = 0 & \langle V_{REC1} V^*_{Ro} \rangle = 0 & \langle V_{REC1} V^*_{REC2} \rangle = 0 \\
\langle V^*_{REC1} V^*_{NR1} \rangle = 0 & \langle V^*_{REC1} V^*_{NR2} \rangle = 0 & \langle V^*_{REC1} V^*_A \rangle = 0 & \langle V^*_{REC1} V^*_{Ro} \rangle = 0 & \langle V^*_{REC1} V^*_{REC2} \rangle = 0 \\
\langle V_{Ro} V^*_{NR1} \rangle = 0 & \langle V_{Ro} V^*_{NR2} \rangle = 0 & \langle V_{Ro} V^*_A \rangle = 0 & \langle V_{Ro} V^*_{REC1} \rangle = 0 & \langle V_{Ro} V^*_{REC2} \rangle = 0 \\
\langle V^*_{Ro} V^*_{NR1} \rangle = 0 & \langle V^*_{Ro} V^*_{NR2} \rangle = 0 & \langle V^*_{Ro} V^*_A \rangle = 0 & \langle V^*_{Ro} V^*_{REC1} \rangle = 0 & \langle V^*_{Ro} V^*_{REC2} \rangle = 0 \\
\langle V_{NR_1} V^*_{NR2} \rangle = 0 & \langle V_{NR_1} V^*_A \rangle = 0 & \langle V_{NR_1} V^*_{Ro} \rangle = 0 & \langle V_{NR_1} V^*_{REC1} \rangle = 0 & \langle V_{NR_1} V^*_{REC2} \rangle = 0 \\
\langle V^*_{NR_1} V^*_{NR2} \rangle = 0 & \langle V^*_{NR_1} V^*_A \rangle = 0 & \langle V^*_{NR_1} V^*_{Ro} \rangle = 0 & \langle V^*_{NR_1} V^*_{REC1} \rangle = 0 & \langle V^*_{NR_1} V^*_{REC2} \rangle = 0 \\
\langle V_{NR_2} V^*_{NR1} \rangle = 0 & \langle V_{NR_2} V^*_A \rangle = 0 & \langle V_{NR_2} V^*_{Ro} \rangle = 0 & \langle V_{NR_2} V^*_{REC1} \rangle = 0 & \langle V_{NR_2} V^*_{REC2} \rangle = 0 \\
\langle V^*_{NR_2} V^*_{NR1} \rangle = 0 & \langle V^*_{NR_2} V^*_A \rangle = 0 & \langle V^*_{NR_2} V^*_{Ro} \rangle = 0 & \langle V^*_{NR_2} V^*_{REC1} \rangle = 0 & \langle V^*_{NR_2} V^*_{REC2} \rangle = 0 \\
\langle V_A V^*_{NR1} \rangle = 0 & \langle V_A V^*_{NR2} \rangle = 0 & \langle V_A V^*_{Ro} \rangle = 0 & \langle V_A V^*_{REC1} \rangle = 0 & \langle V_A V^*_{REC2} \rangle = 0 \\
\langle V^*_A V^*_{NR1} \rangle = 0 & \langle V^*_A V^*_{NR2} \rangle = 0 & \langle V^*_A V^*_{Ro} \rangle = 0 & \langle V^*_A V^*_{REC1} \rangle = 0 & \langle V^*_A V^*_{REC2} \rangle = 0
\end{array}
\tag{2.8}
$$

With the above results, the expressions for the four elements of coherency matrix $\overline{\overline{J_C}}$ can be simplified as follows where $(\theta_I\text{-}\theta_Q) = \Delta\theta$ is the combined path-length error in the transmission network.

$$
\begin{aligned}
c_{11} &= \tfrac{1}{2}|G_{v\pi_1}|^2[2|V_{REC_1}|^2 + (1-|C_{p_1}|^2)|V_{R_0}|^2 + (1-|C_{p_1}|^2)|V_A|^2 + |C_{p_1}|^2|V_{NR_1}|^2 + |C_{p_1}|^2|V_{NR_2}|^2] \\
c_{22} &= \tfrac{1}{2}|G_{v\pi_2}|^2[2|V_{REC_2}|^2 + (1-|C_{p_2}|^2)|V_{R_0}|^2 + (1-|C_{p_2}|^2)|V_A|^2 + |C_{p_2}|^2|V_{NR_1}|^2 + |C_{p_2}|^2|V_{NR_2}|^2] \\
c_{21} &= -\tfrac{1}{2}G^*_{v\pi_1}G_{v\pi_2}e^{j\theta_I}[\sqrt{1-|C_{p_1}|^2}\sqrt{1-|C_{p_2}|^2}\,(|V_A|^2 - |V_{R_0}|^2) - je^{-j\Delta\theta}|C_{p_1}||C_{p_2}|(|V_{NR_1}|^2 - |V_{NR_2}|^2)] \\
c_{12} &= -\tfrac{1}{2}G_{v\pi_1}G^*_{v\pi_2}e^{-j\theta_I}[\sqrt{1-|C_{p_1}|^2}\sqrt{1-|C_{p_2}|^2}\,(|V_A|^2 - |V_{R_0}|^2) + je^{j\Delta\theta}|C_{p_1}||C_{p_2}|(|V_{NR_1}|^2 - |V_{NR_2}|^2)]
\end{aligned}
\tag{2.9}
$$

Rayleigh-Jeans approximation for thermal noise power at microwave frequencies relates noise power generated by a blackbody source to its brightness temperature as follows

$$
\begin{aligned}
\frac{<|V_A|^2>}{R} &= kT_AB & \frac{<|V_{Ro}|^2>}{R} &= kT_{Ro}B \\
\frac{<|V_{NR_1}|^2>}{R} &= kT_{NR_1}B & \frac{<|V_{NR_2}|^2>}{R} &= kT_{NR_2}B \\
\frac{<|V_{REC_1}|^2>}{R} &= kT_{REC_1}B & \frac{<|V_{REC_2}|^2>}{R} &= kT_{REC_2}B
\end{aligned}
\tag{2.10}
$$

Using this approximation, the coherency matrix elements can be written as follows.

$$
\begin{aligned}
c_{11} &= \tfrac{1}{2}|G_{v\pi_1}|^2[2T_{REC_1} + (1-|C_{p_1}|^2)T_{Ro} + (1-|C_{p_1}|^2)T_A + |C_{p_1}|^2T_{NR_1} + |C_{p_1}|^2T_{NR_2}] \\
c_{22} &= \tfrac{1}{2}|G_{v\pi_2}|^2[2T_{REC_2} + (1-|C_{p_2}|^2)T_{Ro} + (1-|C_{p_2}|^2)T_A + |C_{p_2}|^2T_{NR_1} + |C_{p_2}|^2T_{NR_2}] \\
c_{21} &= -\tfrac{1}{2}G^*_{v\pi_1}G_{v\pi_2}e^{j\theta_I}[\sqrt{1-|C_{p_1}|^2}\sqrt{1-|C_{p_2}|^2}\,(T_A - T_{Ro}) - je^{-j\Delta\theta}|C_{p_1}||C_{p_2}|(T_{NR_1} - T_{NR_2})] \\
c_{12} &= -\tfrac{1}{2}G_{v\pi_1}G^*_{v\pi_2}e^{-j\theta_I}[\sqrt{1-|C_{p_1}|^2}\sqrt{1-|C_{p_2}|^2}\,(T_A - T_{Ro}) + je^{j\Delta\theta}|C_{p_1}||C_{p_2}|(T_{NR_1} - T_{NR_2})]
\end{aligned}
\tag{2.11}
$$

2.3 2SQCC Observation Equation and Inversion

The single complex cross correlation expression c_{21} is the observation equation in the 2SQCC architecture.

$$c_{21} = -\frac{1}{2} G^*_{v\pi_1} G_{v\pi_2} e^{j\theta_I} [\sqrt{1-|C_{p_1}|^2}\sqrt{1-|C_{p_2}|^2}(T_A - T_{Ro}) - je^{-j\Delta\theta}|C_{p_1}||C_{p_2}|(T_{NR_1} - T_{NR_2})]$$

Assuming $|C_{p1}| = |C_{p2}| = |C|$ without loss of generality, the expression for c_{21} simplifies to

$$\begin{aligned} c_{21} &= -\frac{1}{2} G^*_{v\pi_1} G_{v\pi_2} e^{j\theta_I} [(1-|C|^2)(T_A - T_{Ro}) - je^{-j\Delta\theta}|C|^2(T_{NR_1} - T_{NR_2})] \\ &= -\frac{1}{2} G^*_{v\pi_1} G_{v\pi_2} e^{j\theta_I} (1-|C|^2)[(T_A - T_{Ro}) - je^{-j\Delta\theta}\frac{|C|^2}{(1-|C|^2)}(T_{NR_1} - T_{NR_2})] \end{aligned} \tag{2.12}$$

Expanding equation 2.12 further using with the relation $-je^{-jx} = -jcos(x) - sin\,(x)$ we get

$$\begin{aligned} c_{21} = -\frac{1}{2} G^*_{v\pi_1} G_{v\pi_2} e^{j\theta_I} (1-|C|^2)[&(T_A - T_{Ro}) - \sin(\Delta\theta)\frac{|C|^2}{(1-|C|^2)}(T_{NR_1} - T_{NR_2}) \\ &- j\cos(\Delta\theta)\frac{|C|^2}{(1-|C|^2)}(T_{NR_1} - T_{NR_2})] \end{aligned} \tag{2.13}$$

It can be observed from equation 2.13 that if the path phase error $\Delta\theta$ is driven to zero, the difference in brightness temperatures input to the quadrature hybrid ($(T_{NR1} - T_{NR2})$ and sum- difference hybrid ($T_A - T_{Ro}$) move orthogonal to each other in the complex correlation space. The two orthogonal axes of brightness temperature differences will be rotated in correlation space by the overall offset angle decided by the phase difference in the individual path amplifier chain gains. The worst-case scenario occurs when the path phase error $\Delta\theta$ is 90° which will cause the brightness temperature differences input to the magic-T and quadrature hybrid to mix linearly and be indistinguishable from each other.

The sufficient statistic of interest in the 2SQCC inversion process to retrieve the antenna temperature T_A is the angle of the complex cross correlation estimate c_{21}. The two complex gain terms can be written as follows

$$G_{v\pi_1} = |G_{v\pi_1}|e^{-j\phi_1} \qquad G^*_{v\pi_1} = |G_{v\pi_1}|e^{+j\phi_1}$$
$$G_{v\pi_2} = |G_{v\pi_2}|e^{-j\phi_2} \qquad G^*_{v\pi_2} = |G_{v\pi_2}|e^{+j\phi_2} \tag{2.14}$$
$$(\phi_1 - \phi_2) = \Delta\phi_{21}$$

The angle of cross correlation estimate c_{21} expressed in 2.13 can then be written as follows.

$$\angle c_{21} = (\Delta\phi_{21} + \theta_I + \pi) - \tan^{-1}\left[\frac{\cos(\Delta\theta)\frac{|C|^2}{(1-|C|^2)}\left(T_{NR_1} - T_{NR_2}\right)}{(T_A - T_{R_0}) - \left[\sin(\Delta\theta)\frac{|C|^2}{(1-|C|^2)}(T_{NR_1} - T_{NR_2})\right]}\right] \tag{2.15}$$

The antenna temperature estimate T_A can be obtained from 2.15 by following the steps below.

$$\tan(\angle c_{21} - (\Delta\phi_{21} + \theta_I + \pi)) = -\frac{\cos(\Delta\theta)\frac{|C|^2}{(1-|C|^2)}\left(T_{NR_1} - T_{NR_2}\right)}{(T_A - T_{R_0}) - \left[\sin(\Delta\theta)\frac{|C|^2}{(1-|C|^2)}(T_{NR_1} - T_{NR_2})\right]} \tag{2.16}$$

$$(T_A - T_{R_0}) - \left[\sin(\Delta\theta)\frac{|C|^2}{(1-|C|^2)}(T_{NR_1} - T_{NR_2})\right] = \frac{-\cos(\Delta\theta)\frac{|C|^2}{(1-|C|^2)}\left(T_{NR_1} - T_{NR_2}\right)}{\tan(\angle c_{21} - (\Delta\phi_{21} + \theta_I + \pi))} \tag{2.17}$$

$$(T_A - T_{R_0}) = \left[\sin(\Delta\theta)\frac{|C|^2}{(1-|C|^2)}(T_{NR_1} - T_{NR_2})\right] - \frac{\cos(\Delta\theta)\frac{|C|^2}{(1-|C|^2)}\left(T_{NR_1} - T_{NR_2}\right)}{\tan(\angle c_{21} - (\Delta\phi_{21} + \theta_I + \pi))} \tag{2.18}$$

$$\boxed{T_A = T_{R_0} + \left[\sin(\Delta\theta)\frac{|C|^2}{(1-|C|^2)}(T_{NR_1} - T_{NR_2})\right] - \frac{\cos(\Delta\theta)\frac{|C|^2}{(1-|C|^2)}\left(T_{NR_1} - T_{NR_2}\right)}{\tan(\angle c_{21} - (\Delta\phi_{21} + \theta_I + \pi))}} \tag{2.19}$$

Equation 2.19 provides a simple estimator expression for retrieving antenna temperature.

2.4 Advantages and Comparative Assessment

In this section, we take a closer look at the estimator expression (2.19) for antenna temperature developed earlier.

$$T_A = T_{R_0} + [\sin(\Delta\theta)\frac{|C|^2}{(1-|C|^2)}(T_{NR_1} - T_{NR_2})] - \frac{\cos(\Delta\theta)\frac{|C|^2}{(1-|C|^2)}(T_{NR_1}-T_{NR_2})}{\tan(\angle c_{21}-(\Delta\phi_{21}+\theta_I+\pi))}$$

T_{Ro} can be set to a fixed reference temperature which can be made stable and measured precisely. The path phase error term $\Delta\theta$ is a hardware parameter that can be measured and adjusted to be close to zero. The phase offset $(\Delta\phi_{21} + \theta_I + \pi)$ is another fixed constant that can be measured using precise VNA measurements. The power output from a noise diode depends only on the diode current. Precise control and knowledge of the noise diode current enables the brightness temperatures T_{NR1} and T_{NR} to be treated as known system constants. The coupling parameter C is another hardware constant that can be precisely measured. T_A is the only unknown parameter in the expression. Therefore, calibration views are not needed in the 2-path 2SQCC MXCR architecture thereby making it a self-calibrating or continuous calibrating instrument. Also, there are no terms in the estimator expression involving the gain of the IF or RF amplifiers thereby making the retrieval robust to amplifier gain fluctuations.

Substituting $C = 0$ in equation 2.13 is equivalent to the 2SQCC architecture being used in the conventional two-path correlating architecture used in COBE, WMAP missions. The two path correlating architecture observation equation is thus

$$c_{21}^{2S} = -\frac{1}{2}G_{v\pi_1}^{*}G_{v\pi_2}e^{j\theta_I}(T_A - T_{Ro}) \tag{2.20}$$

In this 2S architecture, we have one observation equation (given by 2.20) and two unknown parameters - $G_{v\pi1}^{*}G_{v\pi2}$ and T_A. We therefore need at least one calibration view to ensure we have two equations and two unknowns. The gain product of the

two amplifiers is a part of the observation equation requiring additional design considerations to be implemented to minimize gain fluctuations.

The diagonal terms of the coherency matrix, c_{11} and c_{22}, are equivalent to the output of a single path total power radiometer which can be termed as a 1S architecture. Substituting $C = 0$ in the expression for c_{11} in the equation 2.11, the observation equation for the 1S radiometer becomes

$$c_{11}^{1S} = \frac{1}{2}|G_{v\pi_1}|^2[2T_{REC_1} + T_{R_0} + T_A] \tag{2.21}$$

In the 1S architecture, we have unknowns - T_{REC1}, T_A, and $|G_{v\pi 1}|^2$ and only one observation equation given by 2.21. Therefore, for a 1S architecture we need two additional calibration views to determine the gain and offset.

The 2SQCC architecture clearly provides two distinct advantages over the conventional single path total power and two-path correlating architecture.

1) Calibration views are not needed, thereby improving scene time.

2) Retrieval errors due to amplifier gain fluctuations are eliminated.

CHAPTER 3

TRANSMISSION NETWORK NON-IDEALITIES

3.1 Modified 2SQCC Observation Equation

The transmission coefficients of the sum-difference hybrid and the quadrature hybrid were assumed ideal and lossless in the analysis presented in Chapter 2 with a theoretical 3dB power split across all frequencies. To account for the losses and frequency dependencies of the forward transmission parameters, the transmission network can be rewritten as follows.

$$\bar{\bar{T}} = \begin{bmatrix} -j|C_{p_1}| & \sqrt{1-|C_{p_1}|^2} & 0 & 0 \\ 0 & 0 & \sqrt{1-|C_{p_2}|^2} & -j|C_{p_2}| \end{bmatrix} \begin{bmatrix} 0 & 0 & e^{-j\theta_Q} & 0 \\ e^{-j\theta_I} & 0 & 0 & 0 \\ 0 & 1 & 0 & 0 \\ 0 & 0 & 0 & e^{-j\pi} \end{bmatrix} \begin{bmatrix} |M_{11}| & |M_{12}| & 0 & 0 \\ -|M_{21}| & |M_{22}| & 0 & 0 \\ 0 & 0 & |Q_{11}| & -j|Q_{12}| \\ 0 & 0 & -j|Q_{21}| & |Q_{22}| \end{bmatrix} \quad (3.1)$$

The magnitude of the magic-T forward transmission parameters is written as $|M_{ij}|$ and that of the quadrature hybrid is written as $|Q_{ij}|$. Setting $|M_{ij}| = |Q_{ij}| = \frac{1}{\sqrt{2}}$ gives back the ideal transmission network equation of expressed in equation (2.1). The complex FFT coefficients of the two receiver path voltages for the non-ideal transmission network can then be written as follows.

$$\begin{bmatrix} C_1 \\ C_2 \end{bmatrix} = \begin{bmatrix} G_{v\pi_1}\left(e^{-j\theta_I}\sqrt{1-|C_{p_1}|^2}\,(|M_{12}|V_{Ro}+V_A|M_{11}|) - je^{-j\theta_Q}|C_{p_1}|(|Q_{11}|V_{NR_1} - j|Q_{12}|V_{NR_2}) + V_{REC_1}\right) \\ G_{v\pi_2}\left(\sqrt{1-|C_{p_2}|^2}\,(|M_{22}|V_{Ro}-V_A|M_{21}|) + j|C_{p_2}|(|Q_{22}|V_{NR_2} - j|Q_{21}|V_{NR_1}) + V_{REC_2}\right) \end{bmatrix} \quad (3.2)$$

Computing the coherency matrix elements for the non-ideal transmission network case following the similar procedure as before yields the following expressions given below in (3.3). The brightness temperatures at the four input ports are scaled based on the losses in the corresponding transmission path.

$$c_{11} = |G_{v\pi_1}|^2[|M_{11}|^2(1-|C_{p_1}|^2)|V_A|^2 + |M_{12}|^2(1-|C_{p_1}|^2)|V_{R_0}|^2 + |C_{p_1}|^2|Q_{11}|^2|V_{NR_1}|^2 + |C_{p_1}|^2|Q_{12}|^2|V_{NR_2}|^2 + |V_{REC_1}|^2]$$

$$c_{22} = |G_{v\pi_2}|^2[|M_{21}|^2(1-|C_{p_2}|^2)|V_A|^2 + |M_{22}|^2(1-|C_{p_2}|^2)|V_{R_0}|^2 + |C_{p_2}|^2|Q_{21}|^2|V_{NR_1}|^2 + |C_{p_2}|^2|Q_{22}|^2|V_{NR_2}|^2 + |V_{REC_2}|^2]$$

$$\begin{aligned} c_{21} = -G^*_{v\pi_1}G_{v\pi_2}e^{j\theta_I}[&(|M_{11}|\sqrt{1-|C_{p_1}|^2}\,M_{21}\sqrt{1-|C_{p_2}|^2}\,|V_A|^2 - |M_{12}|\sqrt{1-|C_{p_1}|^2}\,|M_{22}|\sqrt{1-|C_{p_2}|^2}\,|V_{R_0}|^2) \\ &- je^{-j\Delta\theta}(|C_{p_1}||Q_{11}||C_{p_2}||Q_{21}||V_{NR_1}|^2 - |C_{p_1}||Q_{12}||C_{p_2}||Q_{22}||V_{NR_2}|^2)] \end{aligned} \quad (3.3)$$

$$\begin{aligned} c_{12} = -G^*_{v\pi_1}G_{v\pi_2}e^{-j\theta_I}[&(|M_{11}|\sqrt{1-|C_{p_1}|^2}\,M_{21}\sqrt{1-|C_{p_2}|^2}\,|V_A|^2 - |M_{12}|\sqrt{1-|C_{p_1}|^2}\,|M_{22}|\sqrt{1-|C_{p_2}|^2}\,|V_{R_0}|^2) \\ &+ je^{j\Delta\theta}(|C_{p_1}||Q_{11}||C_{p_2}||Q_{21}||V_{NR_1}|^2 - |C_{p_1}||Q_{12}||C_{p_2}||Q_{22}||V_{NR_2}|^2)] \end{aligned}$$

Following the port numbering scheme adopted in Figure.2.1, ports 5 and 6 correspond to transmission network's path-1 and path-2 output ports. Ports 1 and 2 correspond to the difference and sum ports of the magic-T which are input ports I1 and I2. Ports 3 and 4 correspond to the two input ports of the quadrature hybrid, I3 and I4. The scaling factors applied to the four input brightness temperatures can be related to the corresponding s-matrix entries as follows.

$$\begin{aligned} |s_{51}| &= |M_{11}|\sqrt{1-|C_{p_1}|^2} & |s_{61}| &= M_{21}\sqrt{1-|C_{p_2}|^2} \\ |s_{52}| &= |M_{12}|\sqrt{1-|C_{p_1}|^2} & |s_{62}| &= |M_{22}|\sqrt{1-|C_{p_2}|^2} \\ |s_{53}| &= |C_{p_1}||Q_{11}| & |s_{63}| &= |C_{p_2}||Q_{21}| \\ |s_{54}| &= |C_{p_1}||Q_{12}| & |s_{64}| &= |C_{p_2}||Q_{22}| \end{aligned} \quad (3.4)$$

Substituting the above scaling factors back to the expression for coherency matrix elements for a non-ideal transmission network and applying Rayleigh-Jeans approximations of equation 2.10, we get

$$\begin{aligned} c_{11} &= |G_{v\pi_1}|^2[|s_{51}|^2T_A + |s_{52}|^2T_{Ro} + |s_{53}|^2T_{NR_1} + |s_{54}|^2T_{NR_2} + T_{REC_1}] \\ c_{22} &= |G_{v\pi_2}|^2[|s_{61}|^2T_A + |s_{62}|^2T_{Ro} + |s_{63}|^2T_{NR_1} + |s_{64}|^2T_{NR_2} + T_{REC_2}] \\ c_{21} &= -G^*_{v\pi_1}G_{v\pi_2}e^{j\theta_I}[(|s_{51}||s_{61}|T_A - |s_{52}||s_{62}|T_{Ro}) - je^{-j\Delta\theta}(|s_{53}||s_{63}|T_{NR_1} - |s_{54}||s_{64}|T_{NR_2})] \\ c_{12} &= -G_{v\pi_1}G^*_{v\pi_2}e^{-j\theta_I}[(|s_{51}||s_{61}|T_A - |s_{52}||s_{62}|T_{Ro}) + je^{j\Delta\theta}(|s_{53}||s_{63}|T_{NR_1} - |s_{54}||s_{64}|T_{NR_2})] \end{aligned} \quad (3.5)$$

Let us define the following variables to simplify the expression for c_{21} to for easier arithmetic manipulation.

$$\begin{aligned} |s_{51}||s_{61}| &= a \qquad & |s_{52}||s_{62}| &= b \\ |s_{53}||s_{63}| &= c \qquad & |s_{54}||s_{64}| &= d \end{aligned} \tag{3.6}$$

The observation equation in the case of a non-ideal 2SQCC transmission network then becomes

$$c_{21} = -G^*_{v\pi_1} G_{v\pi_2} e^{j\theta_I}[(aT_A - bT_{Ro}) - je^{-j\Delta\theta}(cT_{NR_1} - dT_{NR_2})] \tag{3.7}$$

Expanding the equation 3.7 further,

$$\begin{aligned} c_{21} = -G^*_{v\pi_1} G_{v\pi_2} e^{j\theta_I}[(aT_A - bT_{Ro}) - \sin(\Delta\theta)(cT_{NR_1} - dT_{NR_2}) \\ - j\cos(\Delta\theta)(cT_{NR_1} - dT_{NR_2})] \end{aligned} \tag{3.8}$$

Following the similar procedure in Chapter 2,

The angle of cross correlation estimate c_{21} can be written as

$$\angle c_{21} = (\Delta\phi_{21} + \theta_I + \pi) - \tan^{-1}\left[\frac{\cos(\Delta\theta)\left(cT_{NR_1} - dT_{NR_2}\right)}{(aT_A - bT_{R_0}) - [\sin(\Delta\theta)(cT_{NR_1} - dT_{NR_2})]}\right] \tag{3.9}$$

The antenna temperature estimate T_A can be written as

$$\boxed{T_A = \frac{1}{a}[bT_{R_0} + \sin(\Delta\theta)(cT_{NR_1} - dT_{NR_2})] - \frac{\cos(\Delta\theta)\left(cT_{NR_1} - dT_{NR_2}\right)}{\tan(\angle c_{21} - (\Delta\phi_{21} + \theta_I + \pi))}} \tag{3.10}$$

3.2 Handling Coherence Offset

The observation equations developed for the ideal and non-ideal 2SQCC transmission networks (equations 2.12 and 3.7 respectively) are reproduced below.

$$c_{21} = -\tfrac{1}{2} G^*_{v\pi_1} G_{v\pi_2} e^{j\theta_I}(1-|C|^2)[(T_A - T_{Ro}) - je^{-j\Delta\theta}\tfrac{|C|^2}{(1-|C|^2)}(T_{NR_1} - T_{NR_2})]$$

$$c_{21} = -G^*_{v\pi_1} G_{v\pi_2} e^{j\theta_I}[(aT_A - bT_{Ro}) - je^{-j\Delta\theta}(cT_{NR_1} - dT_{NR_2})]$$

For the case of equal brightness temperatures present at all four input ports, there is a non-zero residual c_{21} due to the losses in the transmission network. The four scaling coefficients, $a, b, c,$ and d can be estimated using precise VNA measurements and treated as frequency dependent quantities in the retrieval process. These losses from the passive hybrids and couplers are only a function of temperature and hence the offsets can be considered as constant for a specific frequency.

Substituting $T_A = T_{Ro} = T_{NR1} = T_{NR2} = T_{AMB}$ in equation 3.7, gives us the expression for the coherence offset which is defined as Δc_{21}. (3.11)

$$\Delta c_{21} = -G^*_{v\pi_1} G_{v\pi_2} e^{j\theta_I}[(a-b)T_{AMB} - je^{-j(\Delta\theta)}(c-d)T_{AMB}\ ]$$

This Δc_{21} offset is to be removed from all c_{21} estimates measured for nonzero temperature differences before using in the retrieval process.

CHAPTER 4

ESTIMATION PROCEDURE FOR SYSTEM CONSTANTS

One of the advantages of the 2SQCC architecture is that frequent calibration views are not necessary and the fixed system constants can be estimated a priori and used in the retrieval process. In this chapter we will discuss the estimation procedure for the three fixed constants in the estimator equation - 1) Offset angle $(\Delta\phi_{21} + \theta_I)$, 2) Path phase error $\Delta\theta$, and 3) Noise diode temperature T_{NR}. The estimation process involves setting the input brightness temperatures to known non-zero values in the observation equation 3.7 derived in Chapter 3.

4.1 Offset angle $(\Delta\phi_{21} + \theta_I)$ estimation

Step 1 – Setting $T_A = T_{Ro} = T_{NR1} = T_{NR2} = T_{AMB}$ yields the coherence offset Δc_{21}. This can be achieved by pointing the antenna to a microwave absorber target at room temperature, terminating the sum port of the magic-T and turning off the two noise diodes.

$$\Delta c_{21} = -G^*_{v\pi_1} G_{v\pi_2} e^{j\theta_I}[(a-b)T_{AMB} - je^{-j(\Delta\theta)}(c-d)T_{AMB}\ ]$$

Step 2 – Setting $T_A = T_{LN2}$ & $T_{Ro} = T_{NR1} = T_{NR2} = T_{AMB}$ yields a non-zero coherence estimate of c'_{21}. This can be achieved by pointing the antenna to a microwave absorber target immersed in liquid nitrogen (77 K)

$$c'_{21} = -G^*_{v\pi_1} G_{v\pi_2} e^{j\theta_I}[(aT_{LN_2} - bT_{AMB}) - je^{-j(\Delta\theta)}(c-d)T_{AMB})\ ] \tag{4.1}$$

Step 3 – Compute $c'_{21} - \Delta c_{21}$

$$\begin{aligned} c'_{21} - \Delta c_{21} &= -G^*_{v\pi_1} G_{v\pi_2} e^{j\theta_I}[(aT_{LN_2} - bT_{AMB}) - je^{-j(\Delta\theta)}(c-d)T_{AMB})\ ] \\ &\quad + G^*_{v\pi_1} G_{v\pi_2} e^{j\theta_I}[(a-b)T_{AMB} - je^{-j(\Delta\theta)}(c-d)T_{AMB}\ ] \\ &= -G^*_{v\pi_1} G_{v\pi_2} e^{j\theta_I}[(aT_{LN_2} - bT_{AMB}) - (a-b)T_{AMB}] \\ &= -G^*_{v\pi_1} G_{v\pi_2} e^{j\theta_I} a(T_{LN_2} - T_{AMB}) \end{aligned} \tag{4.2}$$

Step 4 – Estimate the angle of the offset compensated coherency estimate

$$\begin{aligned} \angle(c_{21}^{'} - \Delta c_{21}) &= (\phi_1 - \phi_2) + \theta_I \\ &= \Delta\phi_{21} + \theta_I \end{aligned} \tag{4.3}$$

Note that the term π is not present in the above angle estimate because $(T_{LN2} - T_{AMB})$ is a negative number and gets cancelled with the minus sign upfront in the equation 4.2. If the RF and IF components after the transmission network in the two paths are designed symmetrically, this offset angle can be made smaller.

4.2 Path phase error ($\Delta\theta$) estimation

Step 1 – Setting $T_A = T_{Ro} = T_{NR1} = T_{NR2} = T_{AMB}$ yields the coherence offset Δc_{21}. This can be achieved by pointing the antenna to a microwave absorber target at room temperature, terminating the sum port of the magic-T and turning off the two noise diodes.

$$\Delta c_{21} = -G_{v\pi_1}^{*} G_{v\pi_2} e^{j\theta_I}[(a-b)T_{AMB} - je^{-j(\Delta\theta)}(c-d)T_{AMB}\ ] \tag{4.4}$$

Step 2 – Setting $T_A = T_{Ro} = T_{NR2} = T_{AMB}$ and powering only the noise diode in port 3 with a constant current yields a non-zero coherence estimate of $c_{21}^{''}$ since T_{NR1} is a finite positive number much higher than the ambient temperature. The antenna is pointed to a microwave absorber target at room temperature, the sum port of the magic-T is terminated and the noise diode in port 4 is turned off.

$$c_{21}^{''} = -G_{v\pi_1}^{*} G_{v\pi_2} e^{j\theta_I}[(a-b)T_{AMB} - je^{-j(\Delta\theta)}(cT_{NR_1} - dT_{AMB})\ ] \tag{4.5}$$

Step 3 – Compute $c_{21}^{''} - \Delta c_{21}$

$$\begin{aligned} c_{21}^{''} - \Delta c_{21} &= -G_{v\pi_1}^{*} G_{v\pi_2} e^{j\theta_I}[(a-b)T_{AMB} - je^{-j(\Delta\theta)}(cT_{NR_1} - dT_{AMB})\ ] \\ &\quad + G_{v\pi_1}^{*} G_{v\pi_2} e^{j\theta_I}[(a-b)T_{AMB} - je^{-j(\Delta\theta)}(c-d)T_{AMB}\ ] \end{aligned} \tag{4.5}$$

$$\begin{aligned} &= G_{v\pi_1}^{*} G_{v\pi_2} e^{j\theta_I} je^{-j(\Delta\theta)} cT_{NR_1} - G_{v\pi_1}^{*} G_{v\pi_2} e^{j\theta_I} je^{-j(\Delta\theta)} cT_{AMB} \\ &= jG_{v\pi_1}^{*} G_{v\pi_2} e^{j\theta_Q} c(T_{NR_1} - T_{AMB}) \end{aligned}$$

Step 4 – Estimate the angle of the offset compensated coherency estimate

$$\begin{aligned} \angle c_{21}^{''} - \Delta c_{21} &= (\phi_1 - \phi_2) + \theta_Q + \tfrac{\pi}{2} \\ &= \Delta\phi_{21} + \theta_Q + \tfrac{\pi}{2} \end{aligned} \tag{4.6}$$

Step 5 – Subtract the estimated offset angle from the angle computed above in step 4.

$$\begin{aligned} \angle(c_{21}^{'} - \Delta c_{21}) - \angle(c_{21}^{''} - \Delta c_{21}) &= (\Delta\phi_{21} + \theta_I) - (\Delta\phi_{21} + \theta_Q + \tfrac{\pi}{2}) \\ &= \theta_I - \theta_Q - \tfrac{\pi}{2} \\ &= \Delta\theta - \tfrac{\pi}{2} \end{aligned} \tag{4.7}$$

Note that according to equation 4.7, if the path phase error $\Delta\theta$ is zero, the angle between the offset compensated coherence estimates c_{21}'' and c_{21}' will be 90° which is consistent with the theory.

4.3 Noise diode temperature estimation

The expressions for (c_{21}''- Δc_{21}) and (c_{21}'- Δc_{21}) derived for estimating the offset angle and path phase error in sections 4.1 and 4.2 are used again to estimate the noise diode brightness temperature for a given current.

Step 1 – Calculate the ratio of the magnitudes of (c_{21}''- Δc_{21}) and (c_{21}'- Δc_{21}) using equations 4.5 and 4.2 respectively.

$$\begin{aligned} \left| \frac{c_{21}^{''} - \Delta c_{21}}{c_{21}^{'} - \Delta c_{21}} \right| &= \left| \frac{jG_{v\pi_1}^{*} G_{v\pi_2} e^{j\theta_Q} c(T_{NR_1} - T_{AMB})}{-G_{v\pi_1}^{*} G_{v\pi_2} e^{j\theta_I} a(T_{LN2} - T_{AMB})} \right| \\ &= \left| \frac{c(T_{NR_1} - T_{AMB})}{a(T_{AMB} - T_{LN2})} \right| \end{aligned} \tag{4.8}$$

Step 2 – Cross multiplication and rearranging terms yield the expression for T_{NR1} for a specified set current.

$$\boxed{T_{NR_1} = T_{AMB} + \frac{a}{c} \left| \frac{c_{21}^{''} - \Delta c_{21}}{c_{21}^{'} - \Delta c_{21}} \right| (T_{AMB} - T_{LN2})} \tag{4.9}$$

Following similar steps as before, the brightness temperature output by the other noise diode T_{NR2} can be estimated. Let (c_{21}'''- Δc_{21}) be the offset compensated coherency estimate for the condition where the noise diode in port 4 is powered ON with a specific current providing a brightness temperature output of T_{NR2}. The noise diode in port 3 is powered OFF, the antenna is pointed to a microwave absorber target at room temperature and the sum port of the magic-T is terminated. We have the expression for c_{21}'''- Δc_{21} as follows.

$$\begin{aligned} c_{21}''' - \Delta c_{21} &= -G_{v\pi_1}^{*} G_{v\pi_2} e^{j\theta_I}[(a-b)T_{AMB} - je^{-j(\Delta\theta)}(cT_{AMB} - dT_{NR2})\,] \\ &\quad + G_{v\pi_1}^{*} G_{v\pi_2} e^{j\theta_I}[(a-b)T_{AMB} - je^{-j(\Delta\theta)}(c-d)T_{AMB}\,] \\ &= -G_{v\pi_1}^{*} G_{v\pi_2} e^{j\theta_I} je^{-j(\Delta\theta)} dT_{NR_2} + G_{v\pi_1}^{*} G_{v\pi_2} e^{j\theta_I} je^{-j(\Delta\theta)} dT_{AMB} \\ &= -jG_{v\pi_1}^{*} G_{v\pi_2} e^{j\theta_Q} d(T_{NR_2} - T_{AMB}) \end{aligned} \tag{4.10}$$

Calculating the ratio of the magnitudes of (c_{21}''- Δc_{21}) and (c_{21}'- Δc_{21}) using equations 4.10 and 4.2 respectively yields

$$\begin{aligned} \left| \frac{c_{21}''' - \Delta c_{21}}{c_{21}' - \Delta c_{21}} \right| &= \left| \frac{-jG_{v\pi_1}^{*} G_{v\pi_2} e^{j\theta_Q} d(T_{NR_2} - T_{AMB})}{-G_{v\pi_1}^{*} G_{v\pi_2} e^{j\theta_I} a(T_{LN2} - T_{AMB})} \right| \\ &= \left| \frac{d(T_{NR_2} - T_{AMB})}{a(T_{AMB} - T_{LN2})} \right| \end{aligned} \tag{4.11}$$

Cross multiplication and rearranging terms yield the expression for T_{NR2} for a specified set current.

$$\boxed{T_{NR_2} = T_{AMB} + \frac{a}{d}\left| \frac{c_{21}''' - \Delta c_{21}}{c_{21}' - \Delta c_{21}} \right| (T_{AMB} - T_{LN2})} \tag{4.12}$$

CHAPTER 5

2SQCC SPECTROMETER PROTOTYPE BUILD

This chapter discusses the hardware details and build of the 2SQCC spectrometer prototype instrument.

5.1 WR19 RF Front end

The V-band 2SQCC spectrometer RF front end is entirely built using WR-19 waveguide components. The Magic-T, quadrature hybrid, and the quarter wave shim in the transmission network were both procured specifically for this instrument. The horn antenna, RF LNAs, cross guide couplers, Gunn diode LO source, isolators, and 3dB splitter were repurposed from an earlier V-band instrument. The model number and manufacturer details of various front-end components are given in Table-1.

Component	**Manufacturer**	**Model Number**	**Cost**
Magic-T	Eravant	SWM-40360320-19-SB	$ 650
Q-hybrid	Quinstar	QSP-U05408	$ 1550
Cross Guide Couplers	Spacek Labs	X53-19 (two units)	N/A
Noise Source	Spacek Labs	NS 53-6 (two units)	N/A
RF LNA	Spacek Labs	SL-534-20-5	N/A
Gunn LO source	Spacek Labs	GU-482	N/A
RF DSB Mixer	Spacek Labs	M53-5	N/A
Isolator	Ferrit Quasar	4IWN-53-1, 4IWX-53-1	N/A
RF Filter	Spacek Labs	F53-4	N/A
Quarter wave shim	Eravant	SWI-19038-SB	$ 110
Conical Horn antenna	Spacek Labs	Not available	N/A

Table-1 RF front end component details.

The RF front end assembled using the WR-19 components listed above is shown in Figure 5.1. The two RF amplifiers and Gunn LO source are both powered using separate LiPo batteries and low drop out regulator boards to preclude correlated power supply noise from corrupting the measurements. The noise diodes are powered by separate power supplies to be able to adjust and monitor the noise diode current. The max current limit that can be supplied to the noise source without causing permanent damage is +17mA. The Gunn diode oscillator requires +4.55V to provide +10dBm output power at 50.1 GHz and draws approximately 700mA. All the waveguide components are bolted to an aluminum base plate for mechanical stability.

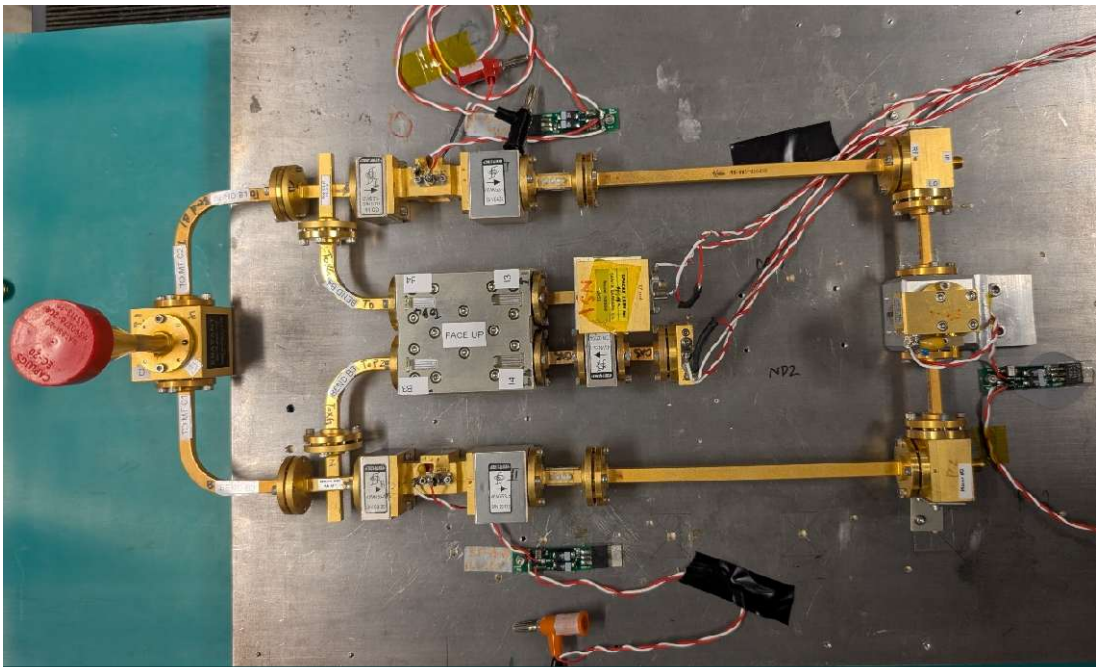

Figure 5.1 2SQCC WR-19 Front end

Component	Voltage (V)	Current (mA)	Power (W)
Gunn LO	4.55	700	3.18
RF Amplifiers	10	80 (40 x 2)	0.80
Noise Diodes	14.5	22 (11 x 2)	0.32
Total	**4.30 W**		

Table 2. Power Consumption by 2SQCC RF front end

5.2 IF Amplification and Filtering

The total IF power available at the mixer output after downconversion from each of the two receiver paths is further amplified by a set of four connectorized Minicircuits GVA-93+ [24] amplifier modules per path. An 8GHz low pass filter is installed right after the RF mixer output to limit the IF bandwidth and avoid spectral folding. A 3dB attenuator is installed between two amplifier modules to improve matching and prevent unwanted oscillations arising from poor amplifier matching. The two amplifier chains need +5V supply voltage and draw +50 mA per amplifier module. Both the IF amplifier chains are powered by a similar scheme as that of the RF section using separate LiPo batteries and linear regulator boards. Figure 5.2 below shows the two IF amplifier chains mounted inside an aluminum box for RF shielding.

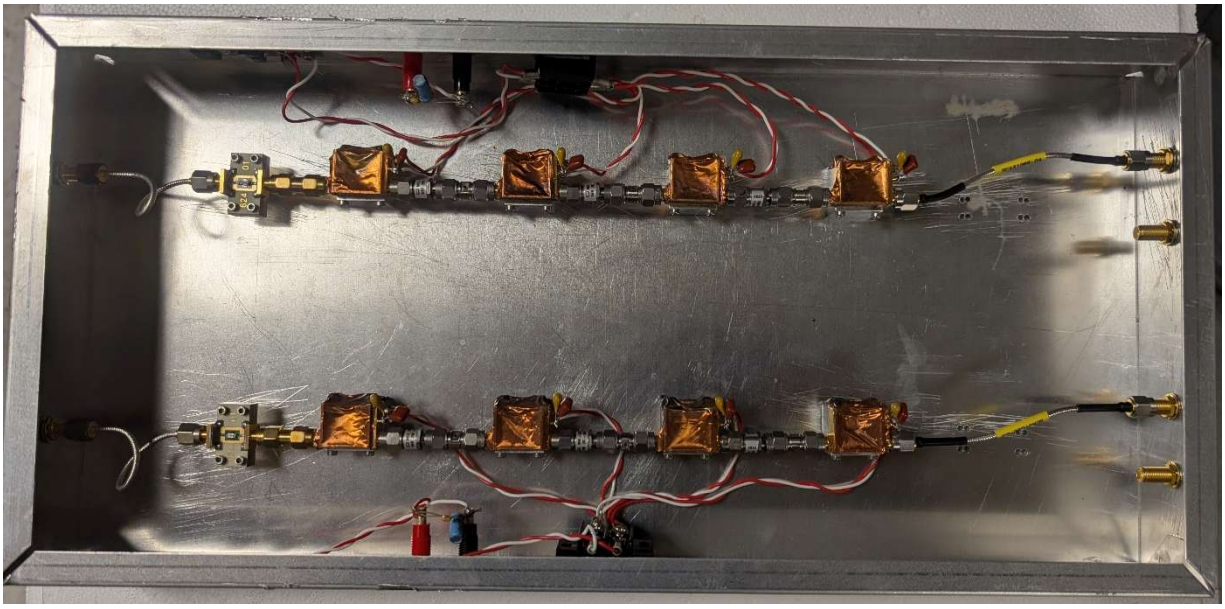

Figure 5.2 Connectorized IF amplifier module

Each of the four GVA-93+ amplifiers in both receiver paths provide +18dB gain. There are three 3dB attenuators in each IF amplifier chain. Hence the total IF gain available in each path is approximately +63 dB. The total power consumption by the IF board is approximately 2 Watts (5V, 200mA x 2).

5.3 High-speed data acquisition

Coherent sampling of the amplified IF signals from the two receiver paths is accomplished using a combination of two product evaluation modules graciously donated by Texas Instruments (TI) Inc. The TI ADC evaluation module card ADC12DJ5200RFEVM [25] has a dual channel 12-bit ADC capable of coherent sampling at 5.2 GS/s and has an analog bandwidth of up to 9 GHz and full-scale input voltage of +4 dBm. The EVM is operated in JMODE3 configuration with external device and reference clocks supplied using a SynthHD pro v2 portable signal generator. The ADC12DJ5200RFEVM is programmable to operate at a specific sampling rate through a software GUI provided by Texas Instruments. The ADC12DJ5200RFEVM consumes ~16W (12V,1.3A) of power.

The raw ADC data is captured at native rate using a high-speed data capture card TI TSW14J57EVM [26] (Figure 5.3). The two modules are connected using an FMC+ connector. The TI HSDC Pro data capture GUI is used to display and store the captured ADC samples as raw binary (bin) files. A MATLAB based automated data capture process is developed to continuously store the raw ADC data captured by the HSDC Pro software using the libraries made available by Texas Instruments. The data capture card consumes ~22W (12V,1.8A) of power.

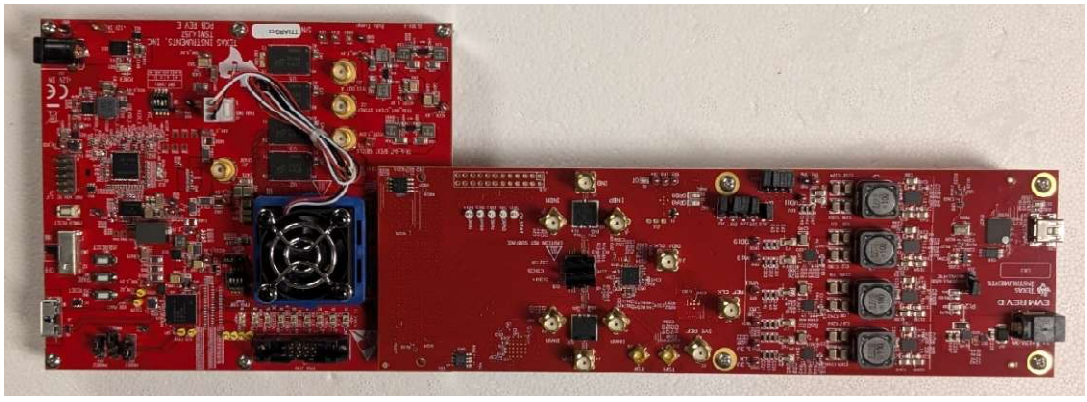

Figure 5.3 Data Capture card TSW14J57EVM (left) and Dual Channel ADC card ADC12DJ5200RFEVM (right)

The 0.1 – 8 GHz IF spectrum is divided to three sub-bands for detection using the ADCs operating at 5.2 GS/s. For the Gunn diode LO frequency of 50.1 GHz, two sub-bands in the RF and IF spectrum are identified as follows. Figure 5.4 shows the frequency response of the filter pairs used to generate sub-bands 1 and 2.

Sub- band #	IF Frequency	RF Frequency	Filter pair used
1	0 – 2.6 GHz	50.1 – 52.7 GHz	VLF-1800+
2	2.6 – 5.2 GHz	52.7 – 55.3 GHz	VBFZ-3590-S+

Table 3. Sub-band mapping using connectorized filter pairs

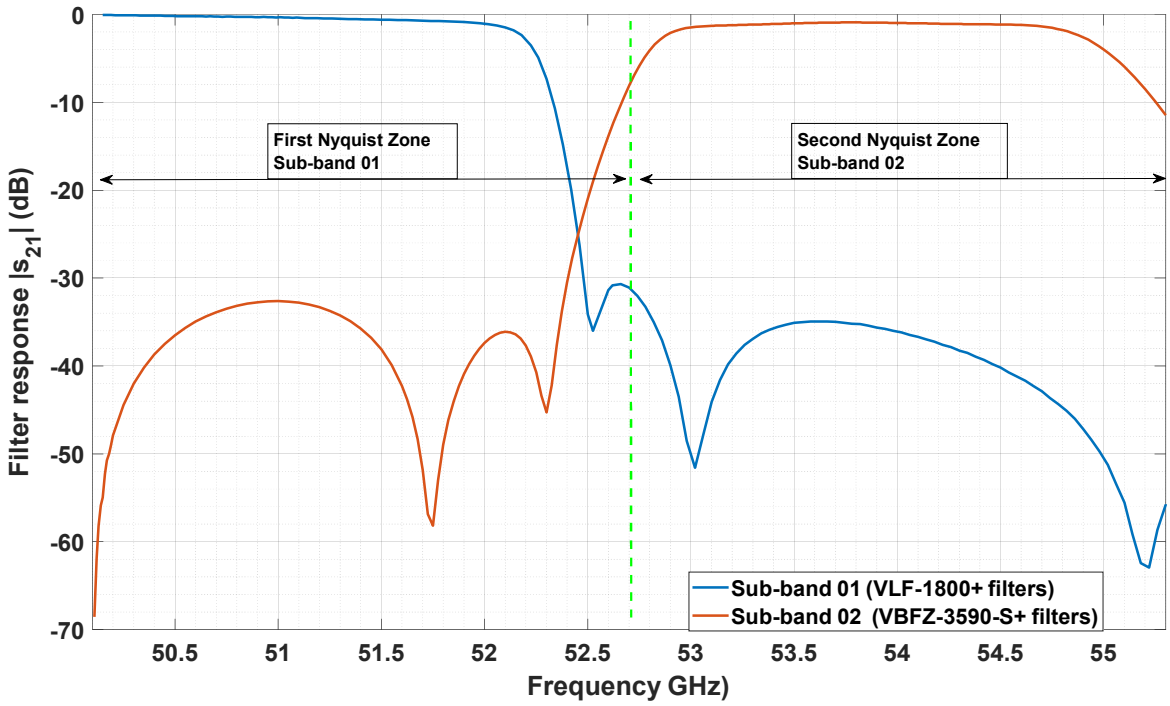

Figure 5.4 IF Sub-banding using connectorized filter pairs. The blue curve represents the passband of the VLF-1800+ filter and the red curve represents the passband of the VBFZ-3590-S+ filter.

5.4 System RF Power Budget

The RF power levels at key points of the 2SQCC spectrometer are given below.

Receiver Noise Temperature per path	1000 K
Scene Temperature	300K
Bandwidth	8 GHz
System Noise Temperature	1000 K + 300 K = 1300 K
Total Power at RF mixer output	-68 dBm (kTsysB)
Total IF Gain	+63 dB
Power loss from sub-banding filtering	-6 dB (8GHz to 2 GHz)
Total power to ADC input ports	-11 dBm
Full scale input power of ADC	+4 dBm
RFI head room before ADC saturation	2.5 bits (15dB power)

Table 4. System RF Power Budget

CHAPTER 6

LABORATORY TESTING & OBSERVATIONS

This chapter discusses the laboratory testing carried out to validate the 2SQCC concept. The discrepancies observed between the theory discussed in Chapters 2-4 and the observations during the testing phase are studied to identify the source of errors.

6.1 Calibration Setup

A custom calibration setup is needed to present the horn antenna with known brightness temperatures to estimate the system constants. Two identical styrofoam enclosures filled with microwave absorber material are used as black body targets. A wooden frame to securely hold the styrofoam enclosure a few inches above the horn antenna aperture is made in house. One of the styrofoam enclosures is filled with liquid nitrogen to act as the cold target (77 K) and the other is kept at room temperature to act as the hot target (Figure 6.1). The walls and lid of the styrofoam enclosure are sealed off with aluminum tape except for a small circular area at the center of the bottom face facing the antenna. This setup ensures that the antenna is only observing the known brightness temperature in the calibration mode.

Figure 6.1 Custom calibration setup built using Styrofoam enclosures and wooden support structure.

6.2 Path phase error estimation and compensation

The fundamental requirement in a 2-path 2SQCC front-end is that the brightness temperature differences input to the sum-difference hybrid and the quadrature hybrid move orthogonal to each other in the correlation space. This requires ensuring precise length matching in building the 2SQCC transmission network hardware. A path phase error of 90° at 50 GHz can occur from a cumulative length mismatch of 1.9mm in the overall transmission network path when using WR19 size waveguides. Length matched waveguide straight sections and bends were used to assemble the transmission network (Figure 6.2).

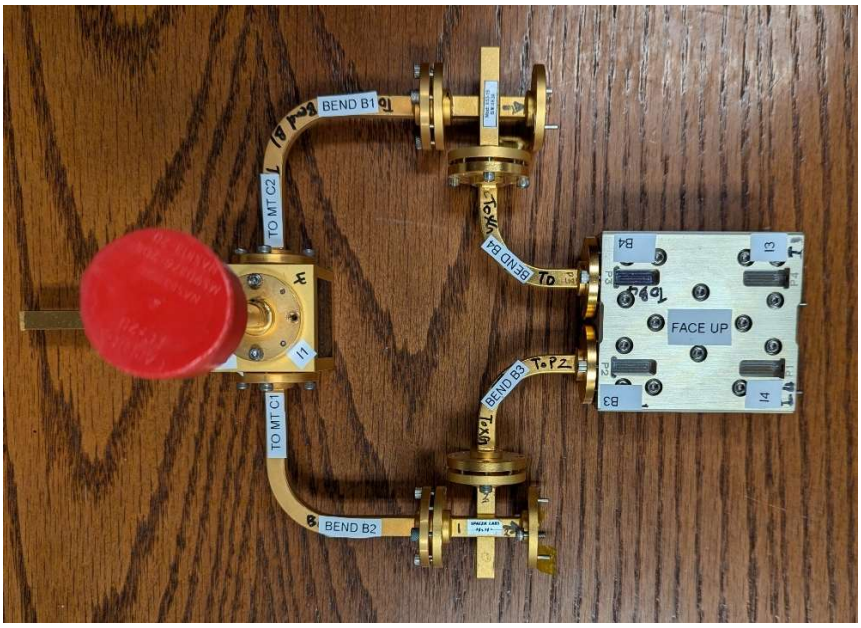

Figure 6.2 2SQCC Transmission Network build using WR19 hardware

Following the procedure described in Chapter 4, the path-phase error in the 2SQCC transmission network in Figure 8 at the front end was estimated. It was observed that the brightness temperature differences in the magic-T and quadrature hybrid were moving in the same axis and were not appearing orthogonal in the correlation space as expected. This can be observed from the scatter plots for c_{21} in the top row in Figure 6.3. The red constellation and purple constellation move along the same

axis contrary to the expected orthogonal movement. This indicated that there is a need for a quarter wavelength shim in the transmission network to ensure orthogonality of brightness temperature differences in the complex correlation space. The scatter plots for c_{21} in the bottom row represent the coherence estimates after the installation of the quarter wave shim. It is clearly seen that the red constellation of points moves orthogonal to the purple and yellow constellations as expected post the installation of the shim.

The yellow constellation of points corresponds to the scatter plot of c_{21} with noise diode 1 turned ON and noise diode 2 OFF. The purple constellation of points corresponds to the scatter plot of c_{21} with noise diode 2 turned ON and noise diode 1 OFF. These two constellations of points move on the same axis opposite to each other as expected for both the sub bands.

The blue constellation of points corresponds to coherence estimate c_{21} for the case of $T_A = T_{Ro} = T_{NR1} = T_{NR2}$ which is defined as the coherency offset Δc_{21} in Chapter 3. For sub-band 01 the coherency offset is very small as evident from the spread of the constellation about the origin. For sub-band 02, the coherency offset is higher, but the orthogonality of brightness temperature differences is preserved.

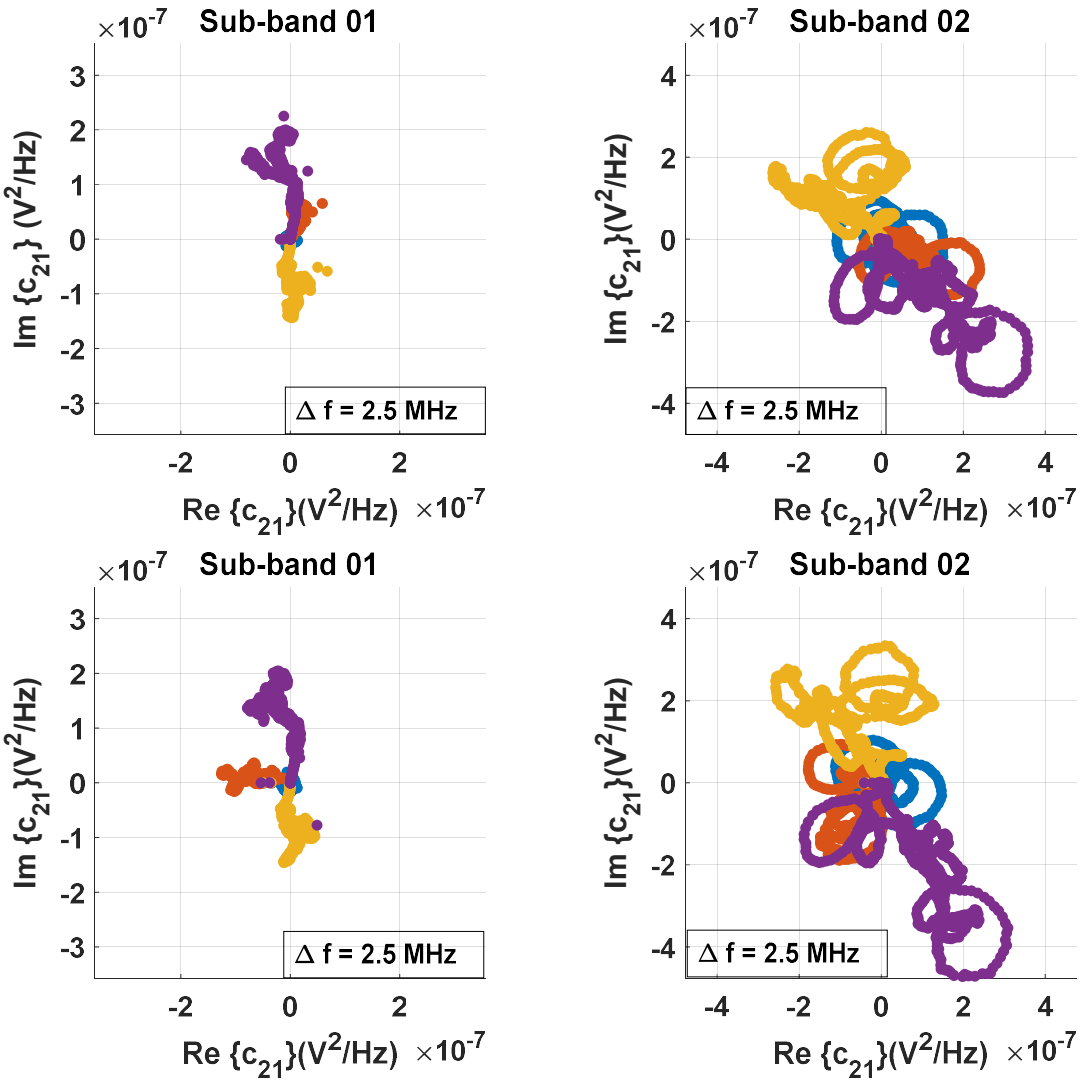

$T_A = T_{R_0}, T_{NR1} = T_{NR2}$ $T_A < T_{R_0}, T_{NR1} = T_{NR2}$

$T_A = T_{R_0}, T_{NR1} > T_{NR2}$ $T_A = T_{R_0}, T_{NR1} < T_{NR2}$

Figure 6.3. Coherency estimate (c_{21}) plots before path phase error compensation (top row) and after path phase error compensation (bottom row). The color-coded legend indicates the brightness temperature conditions generating the corresponding c_{21} estimates.

6.3 Effect of Noise Diode Reflections

A pair of noise diodes are used to provide the reference brightness temperatures T_{NR1} and T_{NR2} input to the quadrature hybrid in the 2SQCC transmission network. Initially, the two noise diodes were directly connected to the quadrature hybrid input ports through a straight section. The two noise diodes unfortunately had very poor s_{11} performance. The return loss improved slightly with an increase in the amount of current flowing through the diode. To ensure a better match so that the reflected power does not cause unwanted coherence offsets, an isolator was installed at the outputs of both of the noise diodes. A waveguide bend had to be used instead of a straight section for one of the isolators due to insufficient mechanical clearance between waveguide ports of the quadrature hybrid (Figure 6.4). The s_{11} plots of both the noise diodes for different currents are given in Figure 6.5.

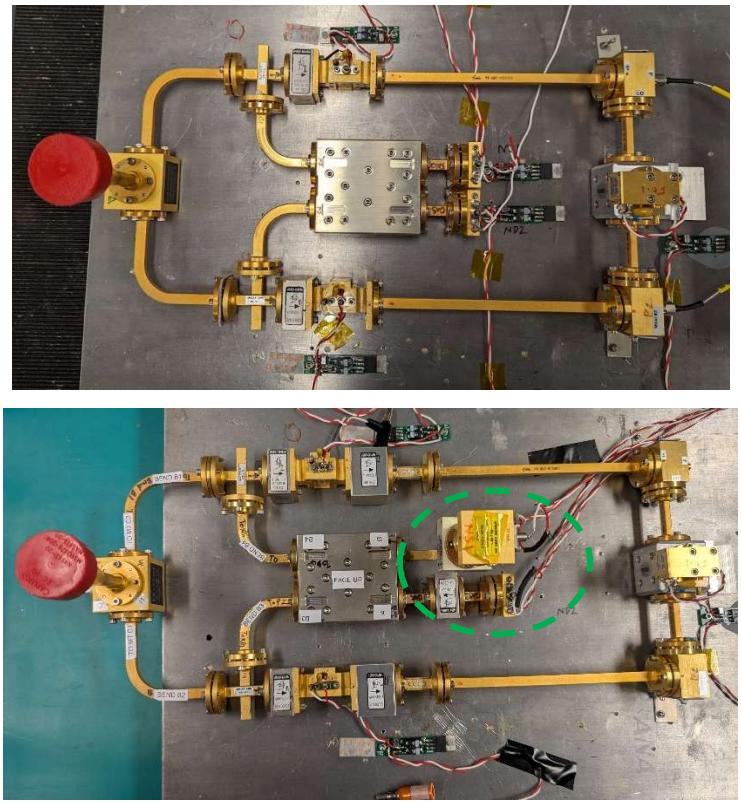

Figure 6.4 Isolator installation (top-before, bottom-after) to improve noise diode matching and minimize reflection induced phase offsets. The circle indicates the location of the isolator.

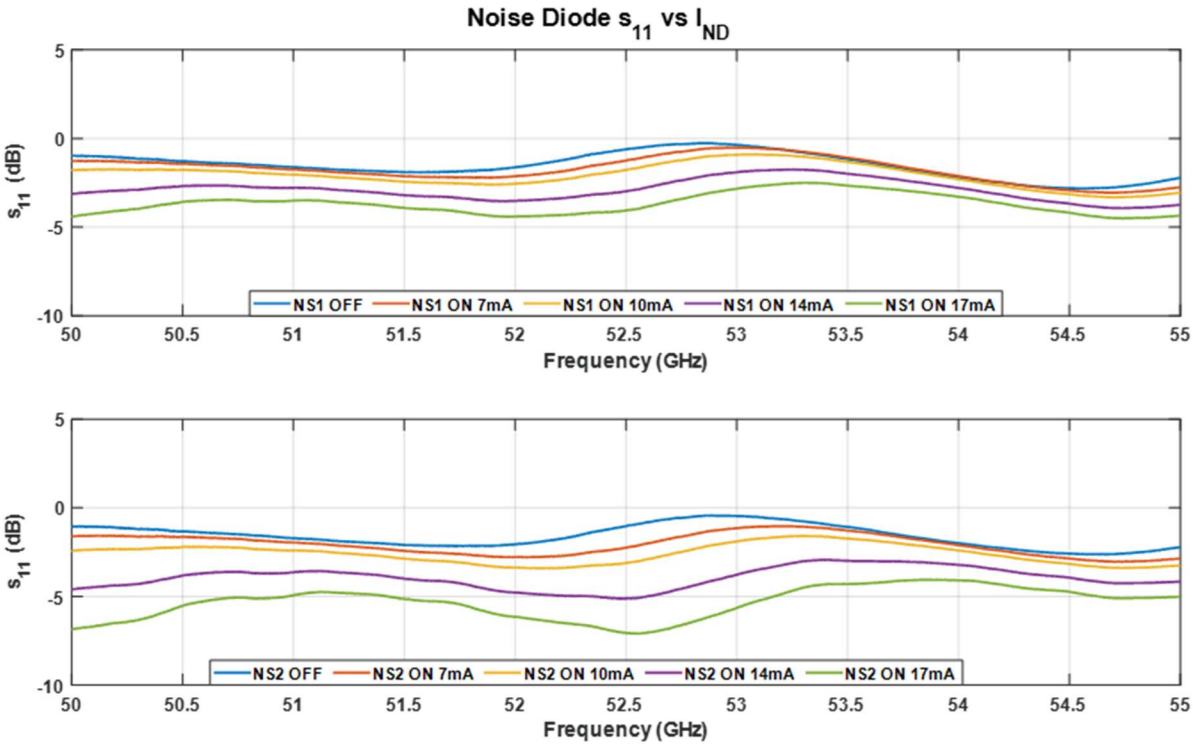

Figure 6.5 Return loss at the noise diode output port for different currents

The installation of the isolators improved the orthogonality of the brightness temperature differences in the correlation space considerably. This is demonstrated in Figure 6.6. Consider the coherence estimate for the case of the brightness temperature difference $\Delta T_R > 0, \Delta T_A = 0$ (Noise Diode 1 ON, purple constellation of points) on both the left and right plots. The orthogonality of the brightness temperature differences improved by ~20° with the installation of the isolators.

It was earlier discussed that the path phase error $\Delta\theta$ is only a function of physical length mismatches in the transmission network. The noise diode reflections due to poor matching resulted in a phase offset error that manifested as path length error compromising the orthogonality of brightness temperature differences. The offset angle $(\Delta\phi_{21} + \theta_I)$ did not change significantly, suggesting the path phase offset was caused purely by noise diode reflections alone and not attributable to the magic-T input ports.

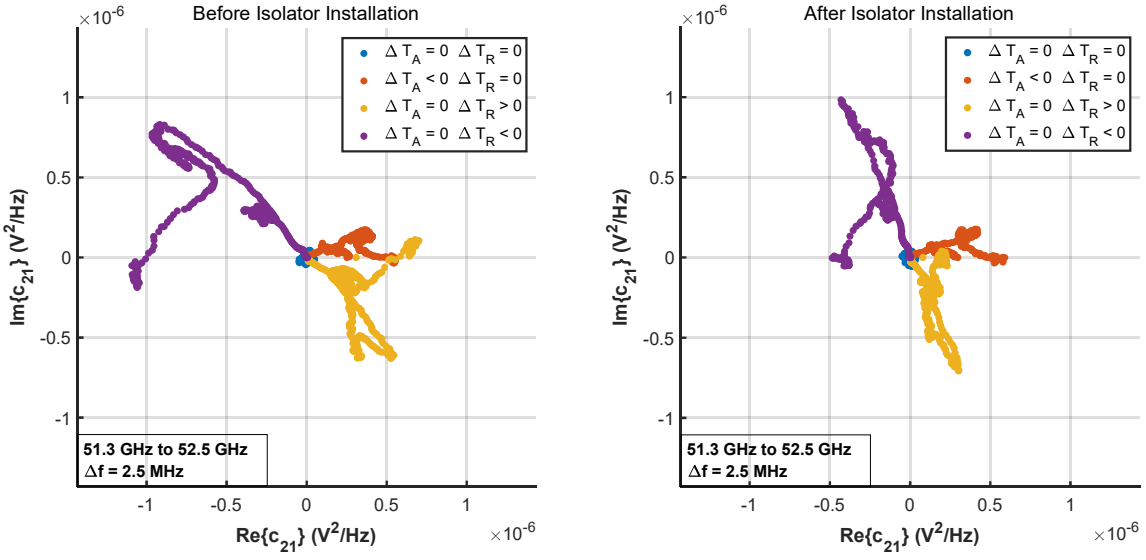

Figure 6.6. Improvement in orthogonality of coherence estimate achieved by isolator installation at noise diode output ports

6.4 Effect of Amplifier Instability

The stability of an RF amplifier is evaluated using the K-factor and/or μ-factor which are in turn derived using s-parameter measurements [27]. Based on the values of these two parameters, circuit stability is classified into different categories. A summary of these stability conditions is given in Table-5.

K-factor	μ-Factor	Circuit Stability
K < 1	μ < 1	Potentially Unstable
K <1	μ >1	Output Potentially Unstable
K > 1	μ < 1	Input Potentially Unstable
K =1	μ = 1	Marginally Stable
K > 1	μ > 1	Unconditionally Stable

Table 5. RF Amplifier Stability conditions based on K and μ factors

It was observed that the RF-LNA on path-01 was potentially unstable over a bandwidth of approximately 1 GHz (54-55 GHz). Both K and μ factors for the RF amplifier in this frequency range was less than 1 (Figure 6.7).

This instability was caused by the poor output matching of the amplifier with the RF filter's input port. To improve matching and make the amplifier unconditionally stable, an isolator was added at the output of the RF LNAs on both the receiver paths. This solved the instability problem and made the path-01 amplifier unconditionally stable. The instability resulted in the path phase offset angle ($\Delta\phi_{21} + \theta_I$) to be different by ~20° before and after the addition of the isolator. The path phase error also moved closer to zero thereby improving the orthogonality of the brightness temperature differences. The coherency c_{21} scatter plot in Figure 6.8 depicts the change in the path phase error and the path phase offset angle caused by the instability and how the installation of the isolator at the amplifier output port improved the overall performance.

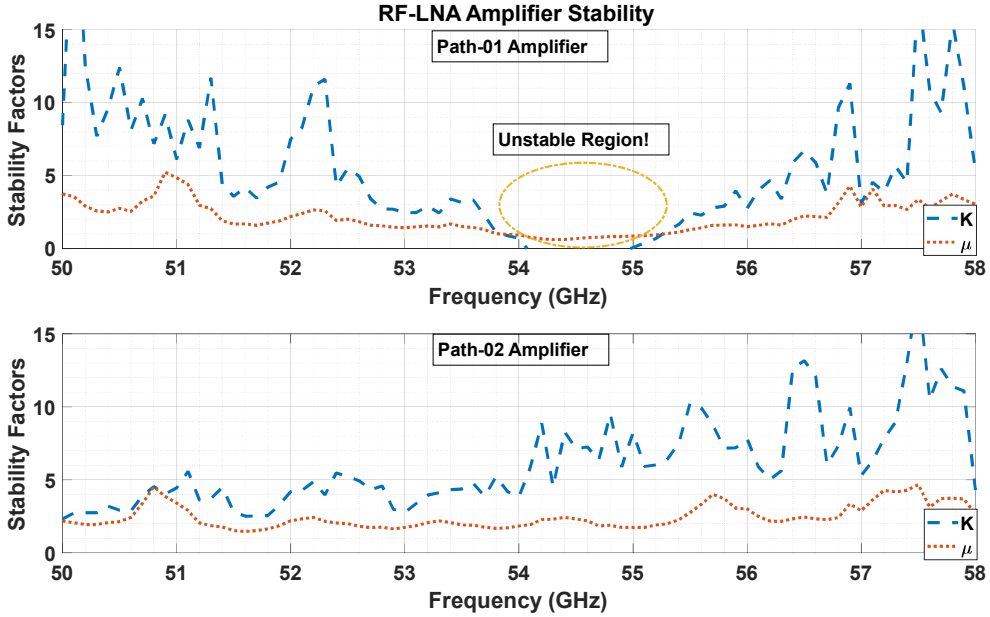

Figure 6.7 Stability factors of RF LNAs

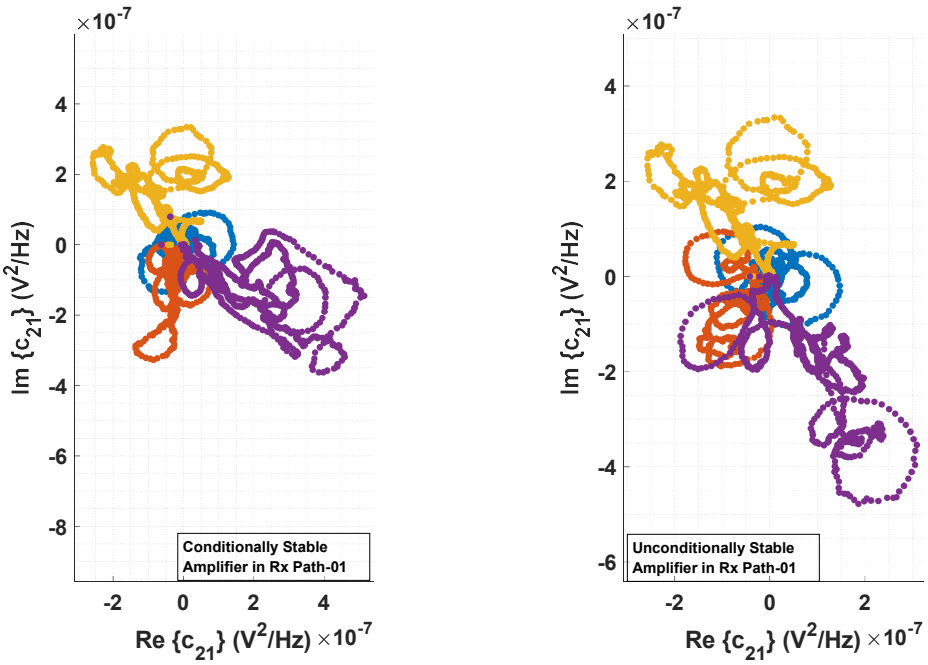

Figure 6.8 c_{21} scatter plot for various input brightness temperature differences. Left (with conditionally stable amplifier in path -01. (Right) unconditionally stable amplifier in path -01.

6.5 Noise Diode Power – Linearity & Repeatability

One of the three parameters that is assumed as a constant in the antenna temperature estimate (equation 2.19) is the noise diode output brightness temperature. The noise diode output power is linearly proportional to the current through the diode. Therefore, by maintaining a constant current drive for the noise diodes, a known stable output brightness temperature from the noise diodes can be obtained. The procedure outlined in section is used to estimate the noise diode output brightness temperature for different current drives for both noise diodes (ND1 and ND2). It is observed that for the same drive current (11mA), the output brightness temperature is constant for different switch ON events on different days. (Figure 6.9). The diode current fluctuated by approximately ±30µA over the course of the data collection period and is the likely source of the slight difference in the output

brightness temperatures observed in the two separate switch ON events. By exercising better current control techniques such as the use of constant current mirror circuits for generating the diode drive current, the diode output brightness temperature can be stabilized much better.

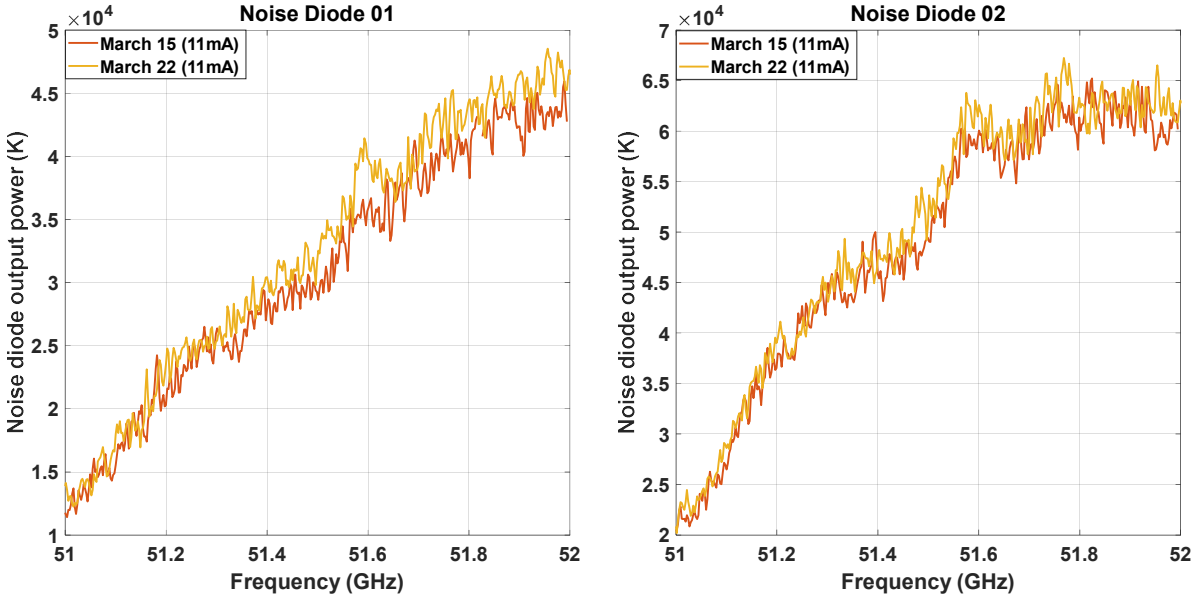

Figure 6.9 Noise diode output brightness temperature (K) for a constant current of 11 mA for different switch ON events. Noise diode 01 (left) and Noise diode 02 (right).

The noise diode output power also scales linearly with the magnitude of the diode current. This characteristic is clearly seen in Figure 6.10 where the noise diode output brightness temperature spectra is estimated for different diode currents (6.5 mA, 11 mA, and 17 mA). The manufacturer specified maximum rated diode current is 17 mA, corresponding to an output Excess Noise Ratio (ENR) of ~23.8dB for noise diode 01 and ~25.37 dB for Noise diode 02. The noise diode is typically operated with a drive current of ~11mA to ensure safety and provide a strong noise signal output from the diode.

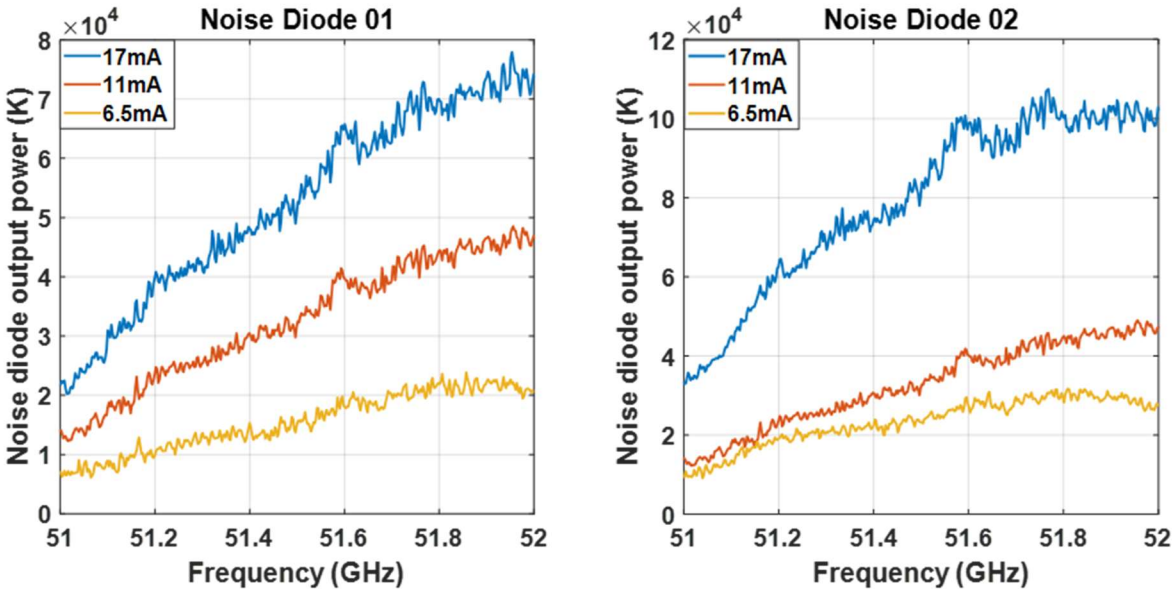

Figure 6.10 Noise diode output brightness temperature (K) different diode drive currents. Noise diode 01 (left) and Noise diode 02 (right).

6.6 Stability of System Constants $(\Delta\phi_{21} + \theta_I)$ and $(\Delta\theta)$

The path phase error $\Delta\theta$ and the path phase offset angle $(\Delta\phi_{21} + \theta_I)$ are treated as fixed hardware constants in the retrieval equation that can be estimated a priori and used in the retrieval process. These two hardware system constants are estimated by presenting known brightness temperature inputs to different ports and following the technique outlined in sections 4.1 and 4.2. Figure 6.11 shows the estimated path phase error computed using data from different switch-ON events and for different diode currents for the frequency range of 51 GHz to 52.5 GHz. As expected, these curves closely follow each other confirming the assumption that the path phase error is indeed a fixed hardware parameter and stays constant. A similar estimation process is used to estimate the path phase offset angle for multiple switch-ON events and this parameter is also found to be a constant validating the assumptions made in using equation 2.19 for retrieval.

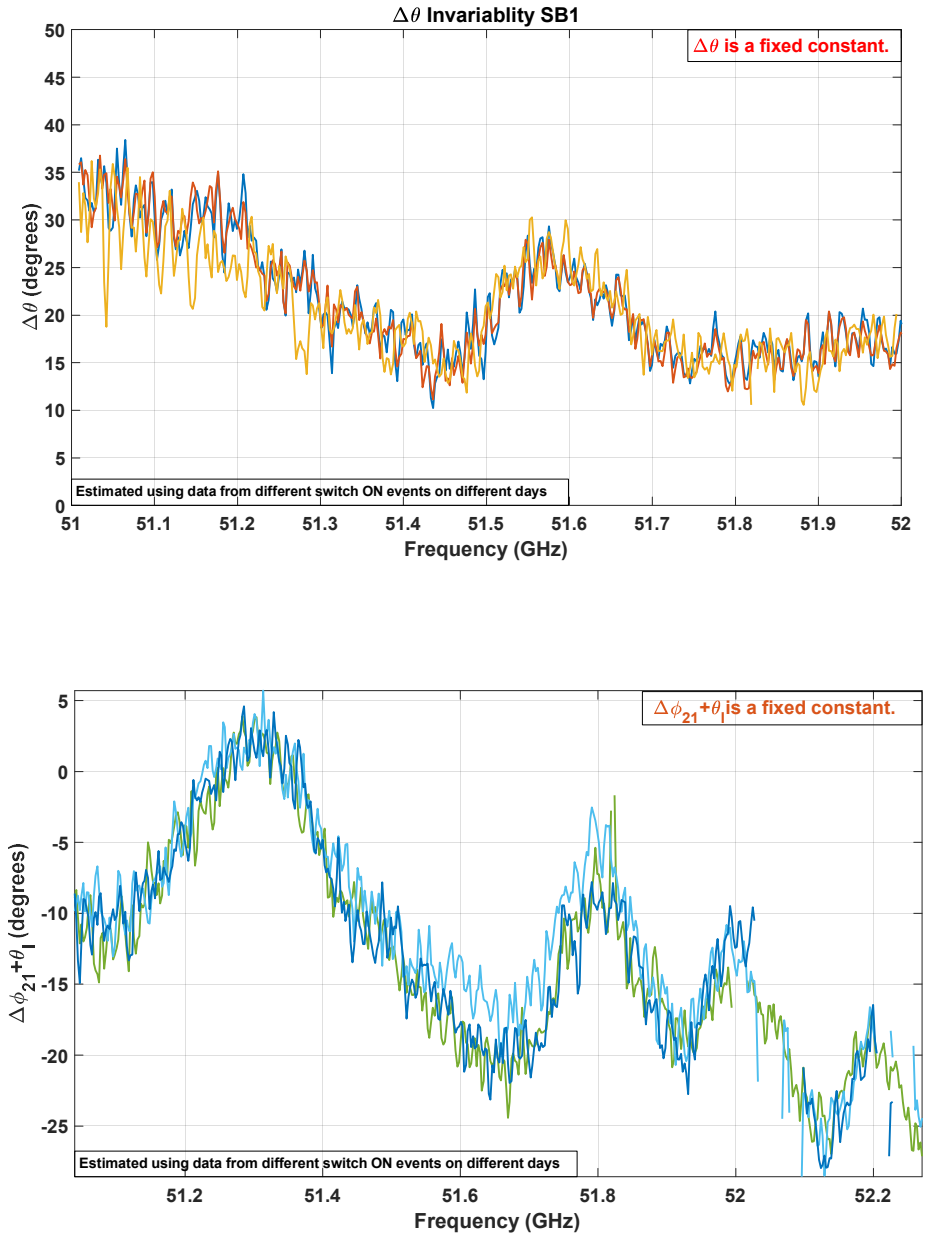

Figure 6.11 The estimated path phase error (top) and the path phase offset angle (bottom) computed using data from different switch ON events.

6.7 Handling Crosstalk

In the mathematical analysis of chapters 2 and 3, the gain matrix was assumed to be a diagonal matrix. This assumption is valid in the absence of any mechanism coupling the signals in one receiver path to the other. In practice, one of the major error mechanisms in a cross-correlating radiometer architecture arises from crosstalk or coupling between the multiple receiver paths. Crosstalk can corrupt the cross-correlation magnitude and angle estimates and introduce systematic errors and offsets into the retrieved geophysical parameter of interest. The amount and mechanism of cross-path coupling are both typically fixed once the hardware is built and need to be quantified and compensated before the detection stage. In a 2SQCC architecture, the cross-talk compensation needs to be applied to the complex FFT coefficients of the two receiver paths before the coherency matrix is computed.

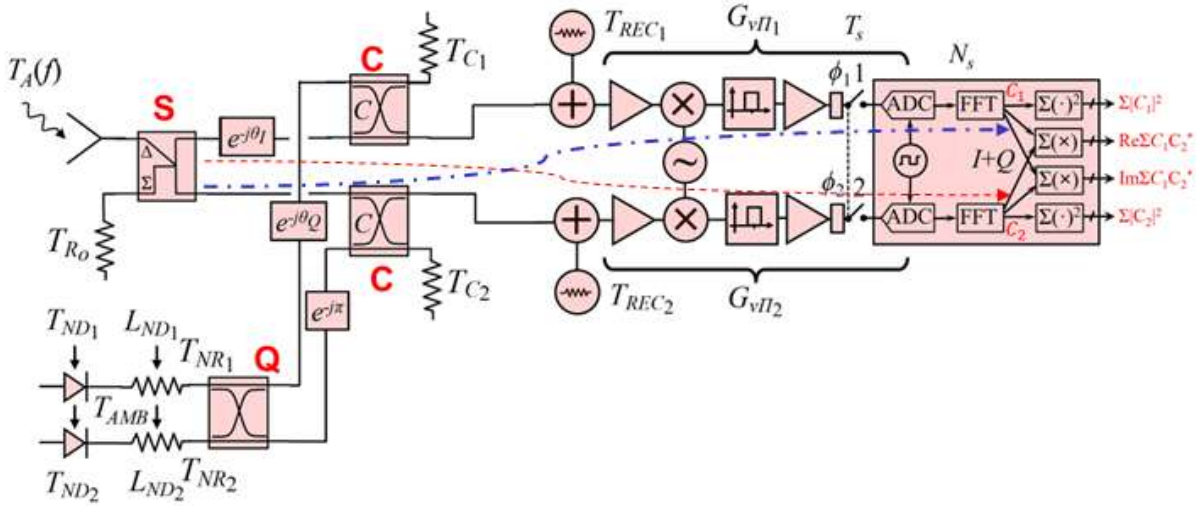

Figure 6.12 Graphical representation of the cross-talk due to coupling between receiver paths. The blue line represents coupling of path-02 signals to path-01. The red line represents coupling of path-01 signals to path-02. The cross-talk can happen at the passive transmission network, RF section, IF section, or at the ADC chip itself.

A mathematical framework to model and compensate for the effects of cross-talk is discussed below. Let C_1^{meas} and C_2^{meas} represent the complex FFT coefficients of the two measured receiver path signals. This can be considered as the combination of the true value that we are seeking mixed with a fraction of the signal coupled from the other path. This mixing process can be modeled as follows.

$$\begin{bmatrix} C_1^{meas} \\ C_2^{meas} \end{bmatrix} = \begin{bmatrix} 1 & H_{x\Pi_{12}} \\ H_{x\Pi_{21}} & 1 \end{bmatrix} \begin{bmatrix} C_1^{true} \\ C_2^{true} \end{bmatrix} = \begin{bmatrix} C_1^{true} + H_{x\Pi_{12}} C_2^{true} \\ C_2^{true} + H_{x\Pi_{12}} C_1^{true} \end{bmatrix} \tag{6.1}$$

$H_{x\Pi_{12}}$ and $H_{x\Pi_{21}}$ represent the coupling coefficients between the two paths and can be different from each other depending on the coupling mechanism between the two receiver paths. $H_{x\Pi_{12}}$ represents the amount of path-02 signal coupled to path-01 and $H_{x\Pi_{21}}$ represents the amount of path-01 signal coupled to path-02. The true value of C_1 and C_2 denoted as C_1^{true} and C_2^{true} in equation 6.1 can be retrieved if the coupling coefficients $H_{x\Pi_{12}}$ and $H_{x\Pi_{21}}$can be measured independently. This correction process can be described mathematically as follows.

$$\begin{bmatrix} C_1^{true} \\ C_2^{true} \end{bmatrix} = \begin{bmatrix} 1 & H_{x\Pi_{12}} \\ H_{x\Pi_{21}} & 1 \end{bmatrix}^{-1} \begin{bmatrix} C_1^{meas} \\ C_2^{meas} \end{bmatrix} \tag{6.2}$$

The cross-talk matrix $H_{x\Pi}$ is frequency dependent and the two off diagonal entries of interest $H_{x\Pi_{12}}$ and $H_{x\Pi_{21}}$ can be estimated by sweeping a CW tone of known input power in one path and estimating the complex FFT coefficients of the signals

observed on the two paths at the same frequency. The ratio of the two complex FFT coefficients gives a measure of the crosstalk between the two receiver paths.

The individual elements of the crosstalk matrix $H_{x\Pi}$ can then be estimated as follows.

$$H_{x\Pi_{21}} = \left\langle \frac{C_2}{C_1} \right\rangle = \frac{1}{N_s} \sum \frac{C_2}{C_1} \tag{6.3}$$

where a known CW tone is input to path-01 RF amplifier.

$$H_{x\Pi_{12}} = \left\langle \frac{C_1}{C_2} \right\rangle = \frac{1}{N_s} \sum \frac{C_1}{C_2} \tag{6.4}$$

where a known CW tone is input to path-02 RF amplifier.

Following the above outlined procedure, the cross-talk matrix for the 2SQCC hardware is estimated for the frequency range of 50.1-52.5 GHz. A model of the cross-talk matrix is generated using linear fitting methods as a function of frequency to be used in retrieval before coherency matrix computation. The measured and modeled plot of the crosstalk matrix elements is given in Figures 6.13 and 6.14.

$H_{x\Pi_{12}}$ and $H_{x\Pi_{21}}$ are both complex numbers very much less than 1 for a system with excellent cross-talk rejection. The crosstalk matrix entries measured for the 2SQCC hardware is better than -40dB for the frequency range that was studied (from 50.1-52.5 GHz). The cross-talk increases after 52.2 GHz, and this can be attributed to the cross-talk in the ADC board itself while operating at higher Nyquist zones. The cross-talk performance is limited by the RF-LO isolation in the two RF mixers in the 2SQCC front end. Each mixer in the RF front end has ~20dB of RF-LO isolation thereby totaling to ~-40dB of isolation between the two signal paths and forms an upper bound on the maximum achievable cross-talk performance.

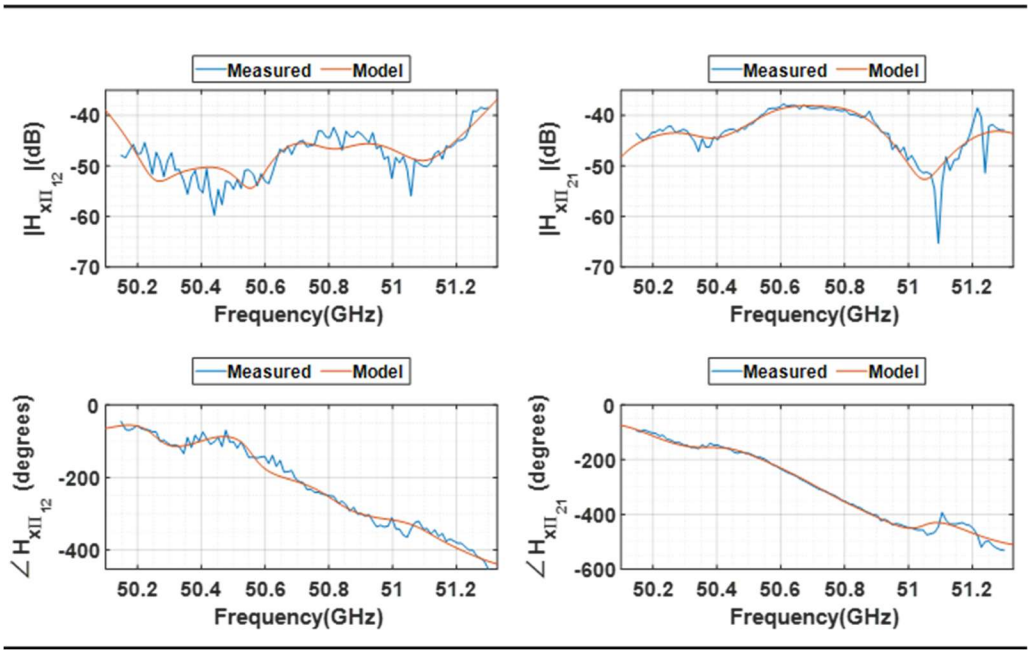

Figure 6.13 Crosstalk matrix element $H_{x\Pi_{12}}$ – Measured & model values.

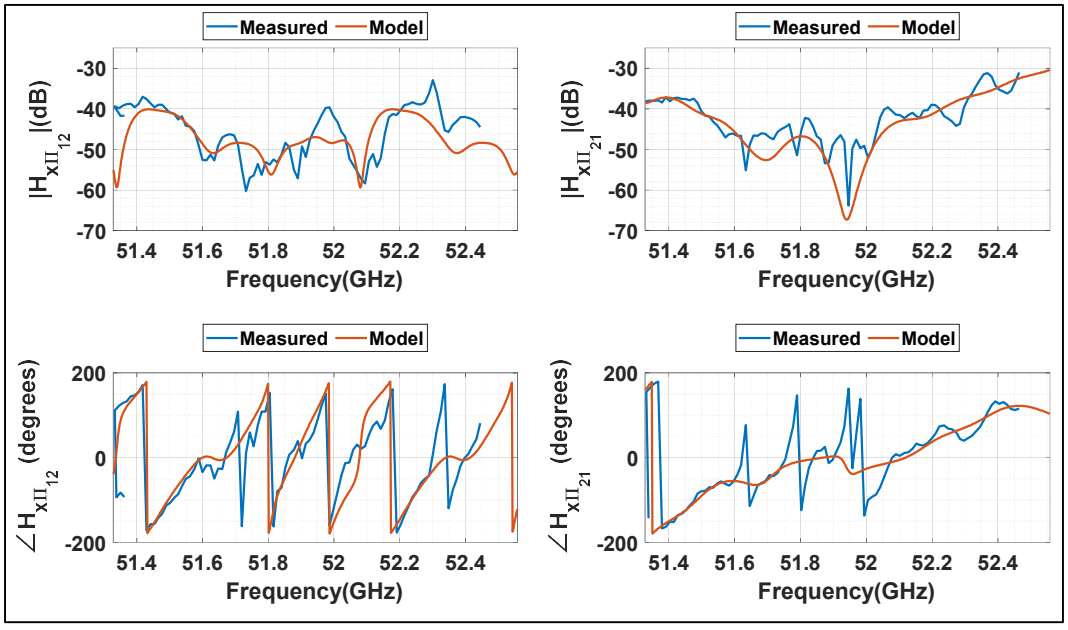

Figure 6.14 Crosstalk matrix element $H_{x\Pi_{21}}$ – Measured & model values.

6.8 VNA Characterization

The discussion in Chapter 3 highlighted the need to account for the non-idealities in the transmission network and derived the expression for coherency matrix elements for a 2SQCC spectrometer with a non-ideal transmission network (equation 3.5). This analysis necessitated a full 6x6 s-matrix VNA characterization of the transmission network to estimate the values of the forward transmission parameters for use in the retrieval equation 3.10 and was performed using the VNA facilities at Weather Stream (Figure 6.15). The port naming convention of Figure 2.1 is followed for this characterization. Since the VNA is a two-port device, fifteen two-port measurements were carried out to generate the full 6x6 S-matrix of the 2SQCC transmission network. The magnitude of the forward transmission parameters for the transmission network measured over a frequency range of 50-58 GHz is shown in Figure 6.16 and will be used in the antenna temperature estimator equation 3.10.

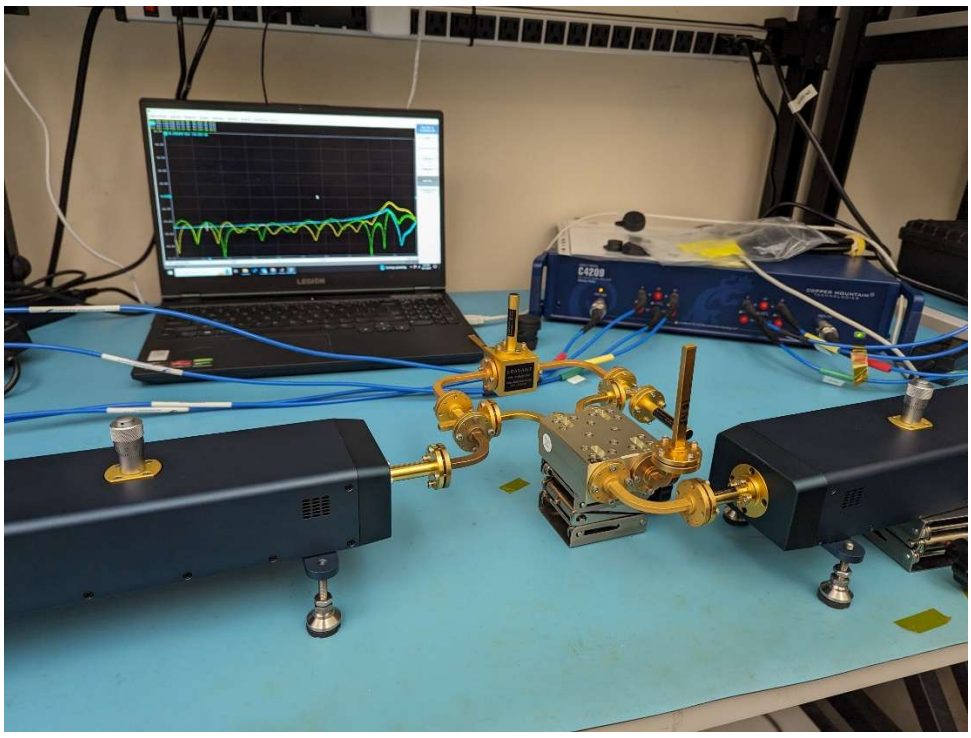

Figure 6.15 Measurement setup for the 2SQCC transmission network VNA characterization.

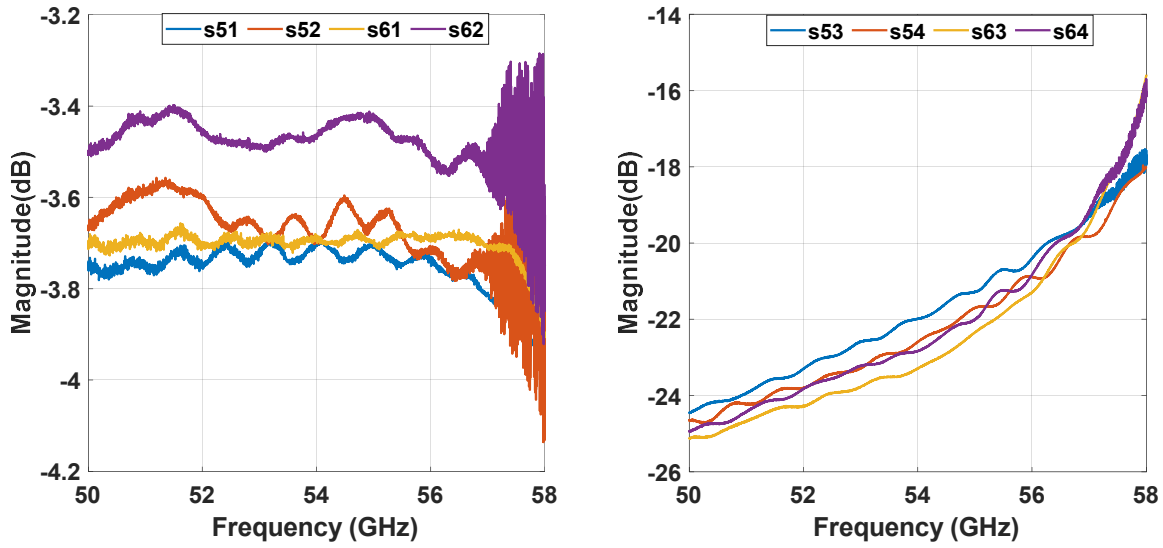

Figure 6.16 2SQCC transmission network forward transmission parameters measured at Weather Stream.

CHAPTER 7

CONCEPT VALIDATION

7.1 Field Testing & Brightness Temperature Retrieval

After the extensive laboratory testing and addressing the challenges discussed in the previous chapters, an outdoor field test was carried out at the University of Colorado campus on March 22, 2025 for concept validation. The microwave brightness temperature spectrum from 50-58 GHz expected to be observed by a zenith pointing spectrometer on a clear sky day at Boulder, CO was generated (Figure 7.1) using the MRT model and an average US standard atmospheric profile [16-18] for comparing the spectra estimated by the 2SQCC spectrometer.

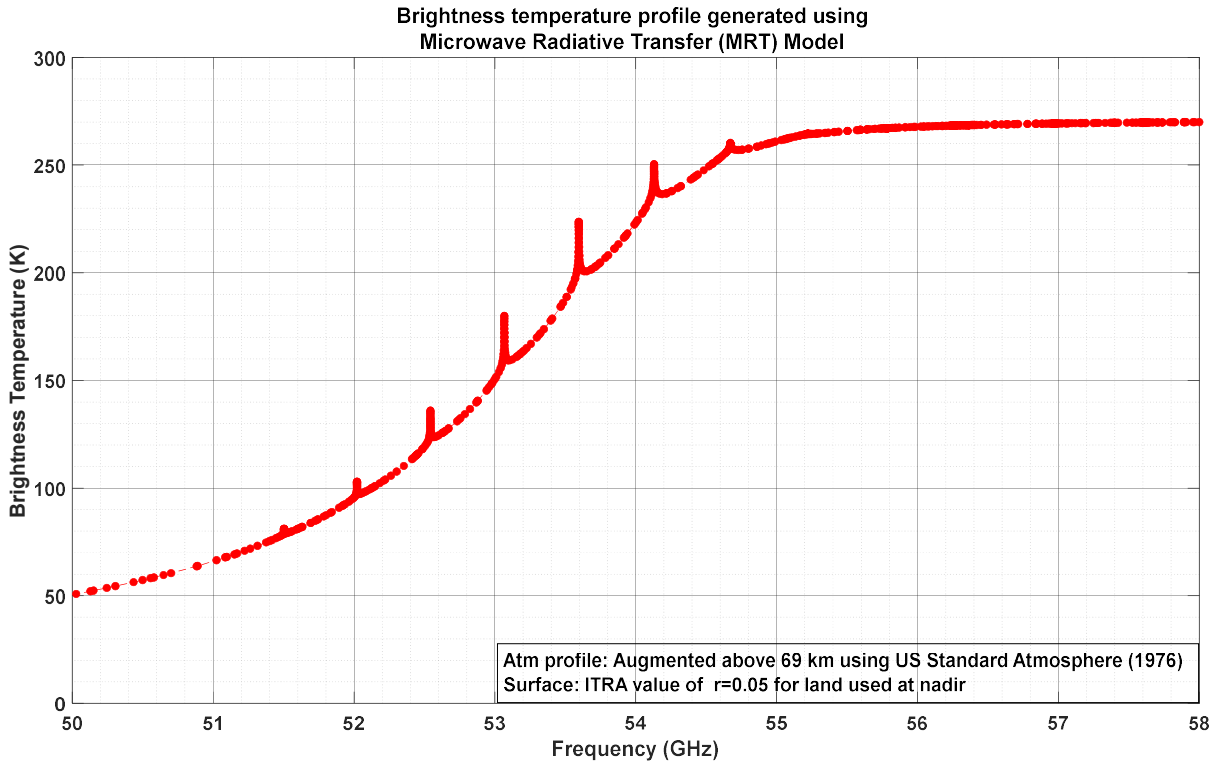

Figure 7.1 Brightness temperature profile generated using MRT model.

The 2SQCC spectrometer and other necessary instrumentation was wheeled over to Farrand Field (Figure 7.2) in a stable four-wheeled cart. The horn antenna was pointed to zenith and sky measurements were taken for both sub-band 01 (50.1-52.7 GHz) and sub-band 02 (52.7 – 55.3 GHz) with the noise diode current set to 11 mA. Only one of the noise diodes were powered ON at a time providing a non-zero brightness temperature difference at the quadrate hybrid input ports. The sum-port of the magic-T was terminated maintaining the same configuration as in the laboratory testing phase.

Figure 7.2 Outdoor Sky measurements with 2SQCC spectrometer (top - left & right). Aravind Venkitasubramony performing the pre-measurement sanity checks and getting the instrument ready for measurements (bottom).

The mathematical procedure for estimating the antenna temperature from the coherence estimate c_{21} was outlined earlier in Chapter 3 which accounted for the different non-idealities in the transmission network. The estimator equation developed in (equation 3.10) for the antenna temperature T_A is reproduced below.

$$T_A = \frac{1}{a}[bT_{R_0} + \sin(\Delta\theta)(cT_{NR_1} - dT_{NR_2})] - \frac{\cos(\Delta\theta)(cT_{NR_1} - dT_{NR_2})}{\tan(\angle c_{21} - (\Delta\phi_{21} + \theta_I + \pi))}]$$

The system constants in the above equation are already estimated from laboratory tests and VNA characterization.

1. Noise diode output brightness temperature T_{NR} (for I=11mA),
2. Path phase error $\Delta\theta$
3. Offset angle $(\Delta\phi_{21} + \theta_I)$
4. Brightness temperature weighting factors $a, b, c,$ and d

Using these constants, the brightness temperature observed by the spectrometer is shown in Figure 7.3 (sub-band 01) and Figure 7.4 (sub-band 02).

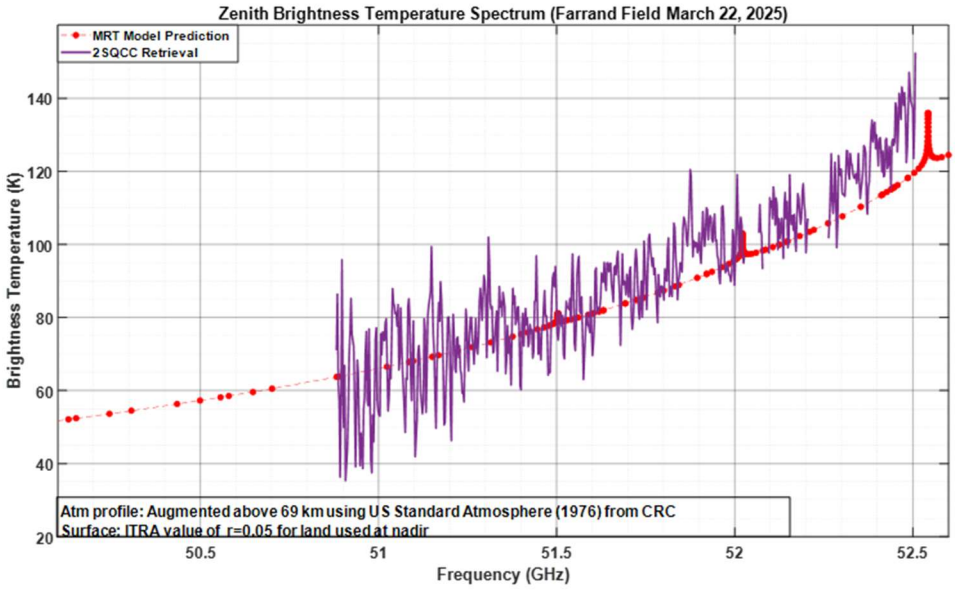

Figure 7.3 Sub-band 01 Brightness temperature spectrum retrieved by 2SQCC spectrometer (purple) and brightness temperature spectrum predicted by MRT model (red)

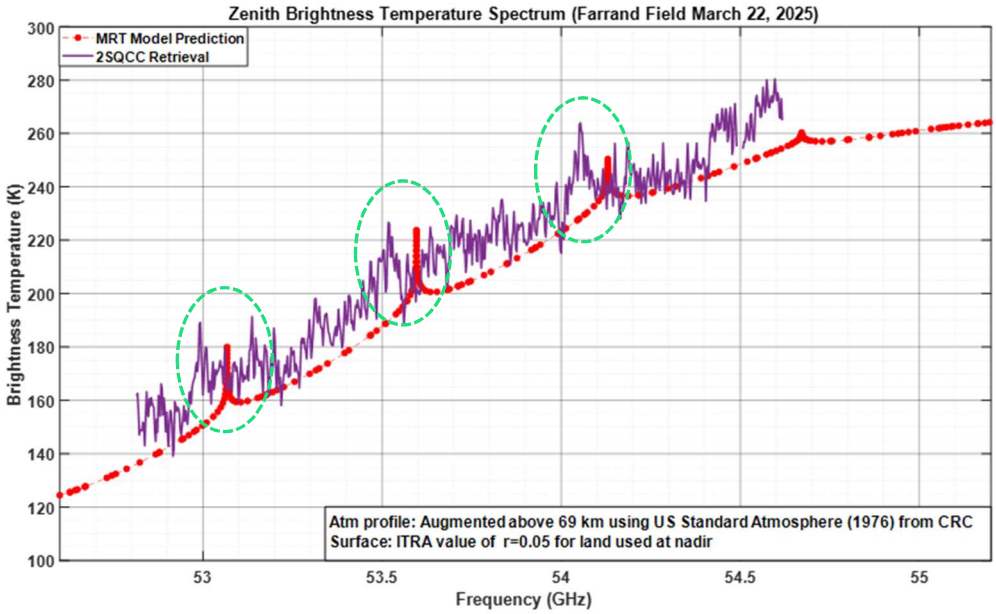

Figure 7.4 Sub-band 02 Brightness temperature spectrum retrieved by 2SQCC spectrometer (purple) and brightness temperature spectrum predicted by MRT model (red). The three green ellipses point out the three absorption peaks in the 53-54.5 GHz region.

The retrieved brightness temperature spectrum is offset from the MRT model prediction by ~7 K which can be attributed to the use of a standard US atmospheric profile in the model and differences in the precise knowledge of the bulk atmospheric temperature on the specific day of the measurement. The three absorption peaks are offset by ~70MHz compared to the model and could be due to the Gunn local oscillator frequency drift. The total data averaged to calculate these estimates is τ_i=51ms with an FFT bin width B= 2.5 MHz.

For a correlating radiometer, the sensitivity ΔT_{rms} is given by the following relation [28]

$$\Delta T_{rms}(correlating) = \frac{\sqrt{2T_{SYS1}T_{SYS2}}}{\sqrt{B\tau_i}} \tag{7.1}$$

Where T_{sys1} and T_{sys2} correspond to the system noise temperatures of the two individual receiver paths. The Y-factor measurements of the two receiver paths

referenced to the antenna aperture yielded receiver noise temperatures T_{REC} for both paths. The average brightness temperature expected to be seen at the horn aperture T_A is obtained from the MRT model. The overall system noise temperature for each individual receiver path referenced to the antenna aperture is thus estimated. (Table 6).

Sub-band #	T_{REC}		T_A		$T_{SYS} = T_A + T_{REC}$	
	Path-01	Path-02	Path-01	Path-02	Path-01	Path-02
Sub-band 01 (50.1-52.7 GHz)	600 K	700 K	100 K	100 K	700 K	800 K
Sub-band 02 (50.1-52.7 GHz)	500 K	500 K	200 K	200 K	700 K	700 K

Table 6. System Noise Temperature estimation for individual receiver paths.

Using equation 7.1, for Sub-band 01, the expected sensitivity of the 2SQCC spectrometer is therefore estimated as 2.97 K. The 6-sigma variation in the measured spectrum is ~30 K and hence the measured ΔT_{rms} is ~5 K. The difference is likely due to the fluctuations in the estimate of the receiver noise temperatures T_{REC1} and T_{REC2}.

Using equation 7.1, for Sub-band 02, the expected sensitivity of the 2SQCC spectrometer is therefore estimated as 2.77 K. The 6-sigma variation in the measured spectrum is ~25 K and hence the measured ΔT_{rms} is ~4.2 K. The performance is slightly better for sub-band 02 as the RF-LNA on both paths is designed for best performance at the center frequency of 53 GHz.

Sub-band #	Theoretical ΔT_{rms}	Measured ΔT_{rms}
Sub-band 01 (50.1-52.7 GHz)	2.97 K	5 K
Sub-band 02 (50.1-52.7 GHz)	2.77 K	4.2 K

Table 7. 2SQCC Spectrometer Sensitivity (Measured vs Expected).

7.2 Comparative Assessment

The measured sensitivity of the 2SQCC spectrometer should be compared against that of an ideal single path total power radiometer for a quantitative comparison of the performance of the new architecture. The sensitivity of a single path total power radiometer is well known [29] and is given by the following relation

$$\Delta T_{rms}(total\ power) = \frac{T_{sys}}{\sqrt{B\tau_i}} \tag{7.2}$$

where T_{sys} is the system noise temperature of the single path radiometer. The diagonal terms of the coherency matrix c_{11} and c_{22} are equivalent to the output of a total power radiometer as evident from the equation 3.5. The brightness temperature estimation using these two terms use only half the total antenna input power due to the 3-dB split at the magic-T. To compensate for that, the brightness temperature estimate using c_{11} and c_{22} are averaged together and used to compare against the sensitivity performance of the 2SQCC spectrometer.

Figure 7.5 shows the brightness temperature spectrum retrieved using the total power method and the 2SQCC method for sub-band 01. The 6-sigma variation in the sub-band 01 spectra retrieved using the total power radiometer method is approximately 20 K and hence the measured sensitivity ΔT_{rms}(total power) is ~3.33 K. The sensitivity of the 2SQCC spectrometer in sub-band 01 was found to be ~5K (Table 7).

Figure 7.6 shows the brightness temperature spectrum retrieved using the total power method and the 2SQCC method for sub-band 02. The 6-sigma variation in the sub-band 02 spectra retrieved using the total power radiometer method is approximately 17 K and hence the measured sensitivity ΔT_{rms}(total power) is ~2.8 K. The sensitivity of the 2SQCC spectrometer in sub-band 01 was found to be ~4.2 K (Table 7).

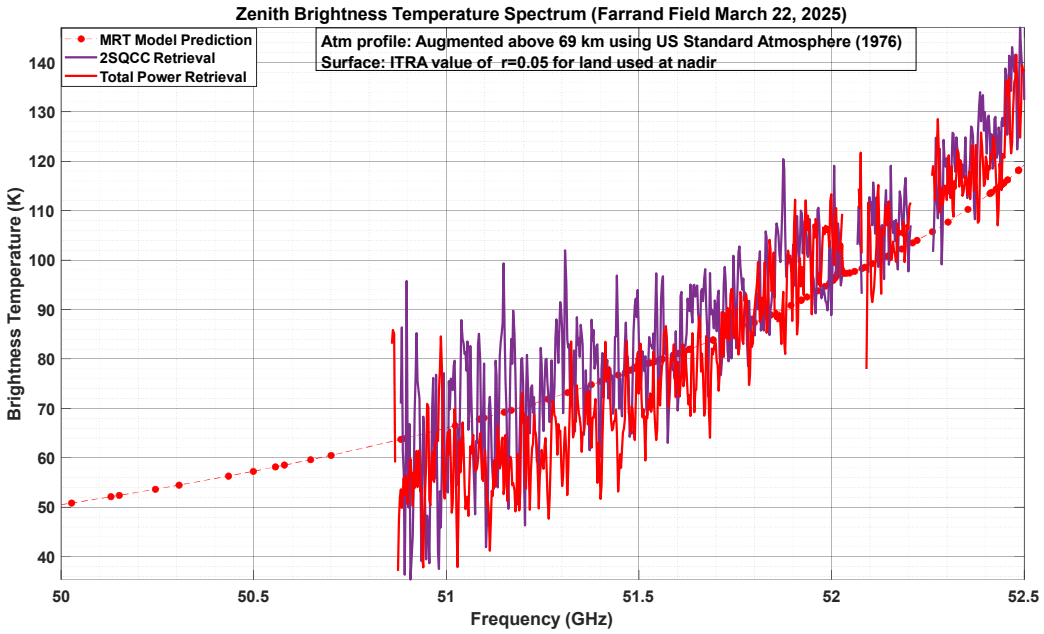

Figure 7.5 Sub-band 01 Brightness temperature spectrum retrieved by 2SQCC spectrometer (purple), brightness temperature spectrum predicted by MRT model (red-dotted), and total power radiometer (red-solid)

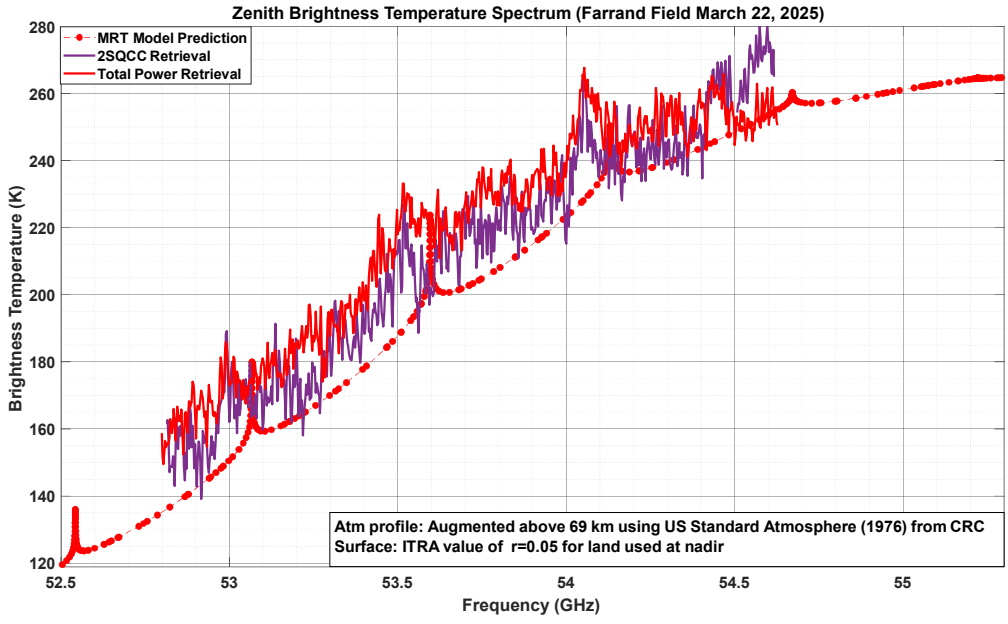

Figure 7.6 Sub-band 02 Brightness temperature spectrum retrieved by 2SQCC spectrometer (purple), brightness temperature spectrum predicted by MRT model (red-dotted), and total power radiometer (red-solid).

Sub-band #	Measured ΔT_{rms} (Total Power)	Measured ΔT_{rms} (2SQCC)
Sub-band 01 (50.1-52.7 GHz)	3.3 K	5.0 K
Sub-band 02 (50.1-52.7 GHz)	2.8 K	4.2 K

Table 8. 2SQCC Retrieval Sensitivity vs Total Power Sensitivity (Measured)

The sensitivity of a total power radiometer is better than the 2SQCC spectrometer. This is along expected lines as the sensitivity of a total power radiometer cannot be theoretically exceeded and is better by a factor of $\sqrt{2}$. The reduction in sensitivity of the 2SQCC MXCR architecture can be compensated by averaging over the additional integration time available as it is continuously calibrating. Dedicated calibration views otherwise required in a total power radiometer for gain and offset estimation are not needed in the 2SQCC architecture and can move closer to the sensitivity of the ideal total power radiometer.

CHAPTER 8

ACTIVE - PASSIVE CO-EXISTENCE THROUGH A SPECTRUM BROKER APPROACH

8.1 RFI Concerns at V-Band & Spectrum Broker Concept

Radio Frequency Interference (RFI) has emerged as a major concern for many users of the electromagnetic spectrum. This is particularly significant in observational sciences—such as radio astronomy, Earth microwave remote sensing, and studies of the Sun and ionosphere—where extremely sensitive measurements are essential. Fifth-generation (5G) wireless communication systems have been assigned frequency bands ranging from 24 to 40 GHz, with specific sub bands detailed in Figure 8.1. However, devices operating in the 24–30 GHz range may inadvertently interfere with water vapor-sensing radiometers—both satellite- and ground-based—that operate in the adjacent 23.6–24.0 GHz band, due to intermodulation effects. Additionally, oxygen-sensing radiometers functioning in the 50–58 GHz band are vulnerable to second-harmonic distortion generated by 5G transmitters in the 24–30 GHz range.

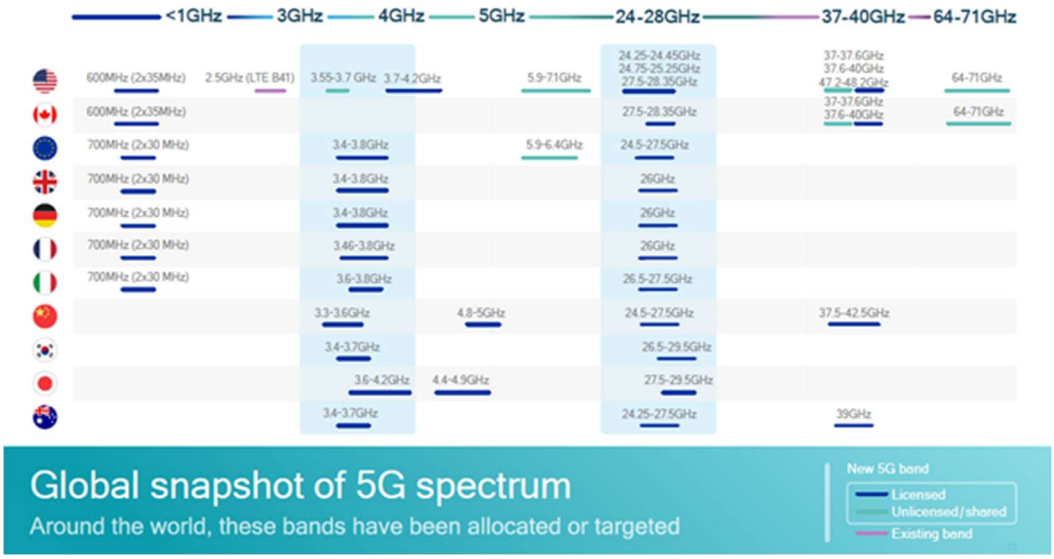

Figure 8.1 Global Fifth Generation (5G) Frequency Allocations (source: Qualcomm)

According to Niiler, NOAA (National Oceanic and Atmospheric Administration) chief Neil Jacobs has warned that interference from 5G transmitters operating near the 24 GHz band could reduce weather forecast accuracy by up to 30 percent—setting forecasting capabilities back to the level of the 1980s [30]. This degradation could pose serious threats to public safety, particularly during hurricanes, tornadoes, and other severe weather events. Lubar adds that such interference could delay the accuracy of a three-day forecast by as much as 3 to 6 hours, significantly increasing the risk to thousands of people in the event of a natural disaster [31].

One strategy to mitigate this interference involves synchronizing terrestrial signal transmissions with short blanking intervals timed precisely with satellite overpasses. Since the exact timing and location of a satellite's beam can be accurately predicted, RFI from 5G sources can potentially be reduced through synchronization-based mitigation.

The concept of a spatial-spectral broker scheme to explore such a co-operative spectrum sharing model and synchronized RFI mitigation approach is explored through a collaborative research effort between three universities – Baylor University, University of Colorado at Boulder, and Purdue University through the NSF Spectrum and Wireless Innovation enabled by Future Technologies (SWIFT) initiative. The 50-58 GHz 2SQCC spectrometer development was partially funded by this project. The spectrometer will be used to report RFI due to second harmonic emissions from a 5G transmitter to the spectrum broker. Upon the report of RFI by the spectrometer, a series of mitigation steps are then initiated by the spectrum broker to minimize interference and ensure co-existence between active and passive users [32].

8.2 Study of RFI from 5G second harmonic emissions

The 4th-order normalized central moment statistic (kurtosis) provides a powerful means of detecting and excising sinusoidal RFI of non-Gaussian anthropogenic origin [33].

$$Kurt(X) = \frac{E(X-\mu)^4}{(E(X-\mu)^2)^2} \tag{8.1}$$

The property that kurtosis of a purely gaussian signal is 3 is very convenient in differentiating the thermal noise of geophysical origin from sinusoidal carrier signals. Since the FFT operation is linear, the real and imaginary parts of the FFT coefficients of a gaussian signal are both gaussian and hence will have a kurtosis equal to $3\pm\Delta K_{rms}$ (where $\Delta K_{rms} = \sqrt{24/N}$ and N is the number of samples used for computing the kurtosis). The MXCR architecture by design works on a spectrometer based digital detection scheme using FFTs to generate the spectrum of the elements of the coherency matrix. The kurtosis of the real and imaginary parts of the individual path FFT coefficients of the 2SQCC spectrometer can be used to generate four kurtosis spectra to report RFI

$$\begin{aligned} SK1_R(f) &= Kurt[\mathrm{Re}\{C_1(f)\}] \\ SK1_I(f) &= Kurt[\mathrm{Im}\{C_1(f)\}] \\ SK2_R(f) &= Kurt[\mathrm{Re}\{C_2(f)\}] \\ SK2_I(f) &= Kurt[\mathrm{Im}\{C_2(f)\}] \end{aligned} \tag{8.2}$$

A spectral RFI mask for each receiver path can be generated using the above four kurtosis spectra to excise RFI corrupted frequency bins in each receiver path. This capability is crucial for all the future passive sensors so that RFI corrupted measurements do not compromise the quality of numerical weather prediction.

A 16-channel COTS 5G beamformer module (TMYTEK BBox-One 5G) [34] and a 16 element 4x4 patch antenna array optimized for use with this unit were procured to mimic a commercial 5G base station (Figure 8.2). The beamformer was driven by a CW tone at 25.25 GHz which would fall in the 5G n258 band. The second harmonic emissions, if any, would appear at 50.5 GHz and can be flagged by the 2SQCC spectrometer using the spectral kurtosis metric and will be reported to the spectrum broker. The test setup block diagram is shown in Figure 8.3.

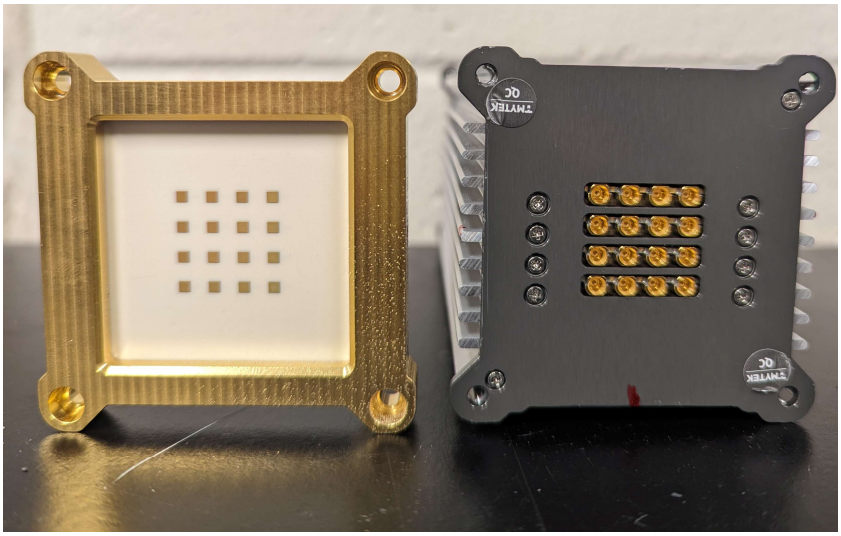

Figure 8.2 TMYTEK BBox-One 5G Beamformer and 4x4 patch antenna array

The BBox transmitter and the receiver horn antenna are separated by 1m distance which ensures that the transmit and receive antennas are in the respective far field zones of each other. Two separate tests were carried out with the test setup in Figure 8.3. For one of the tests, the input signal driving the BBox was generated using a 13GHz signal generator and a frequency doubler (Gigatronix-840). For the second test, the BBox input signal was generated directly from a 40GHz signal generator (HP83640L) without frequency doubler unit.

It was observed that second harmonic emission from the BBox patch antenna array was detected only when the frequency doubler was used to generate the input

signal to the BBox. Whenever the HP83640L signal generator was used to generate the input signal to drive the BBox, the spectrometer did not detect the second harmonic emission. The takeaway from the above test was that the RFI due to second harmonic emission is dependent on the spectral purity of the driving source. The BBox itself did not generate any second harmonic emission. But the second harmonic emission generated by the source itself was able to propagate through the beamformer circuits and radiate through the antenna array. This effect was able to be removed by using a low pass filter of appropriate cutoff frequency at the output of the frequency extender thereby preventing the second harmonic from entering the BBox. Figure 8.4 shows the excision of 50.5 GHz second harmonic signal carried out by a spectral mask generated using the kurtosis spectra.

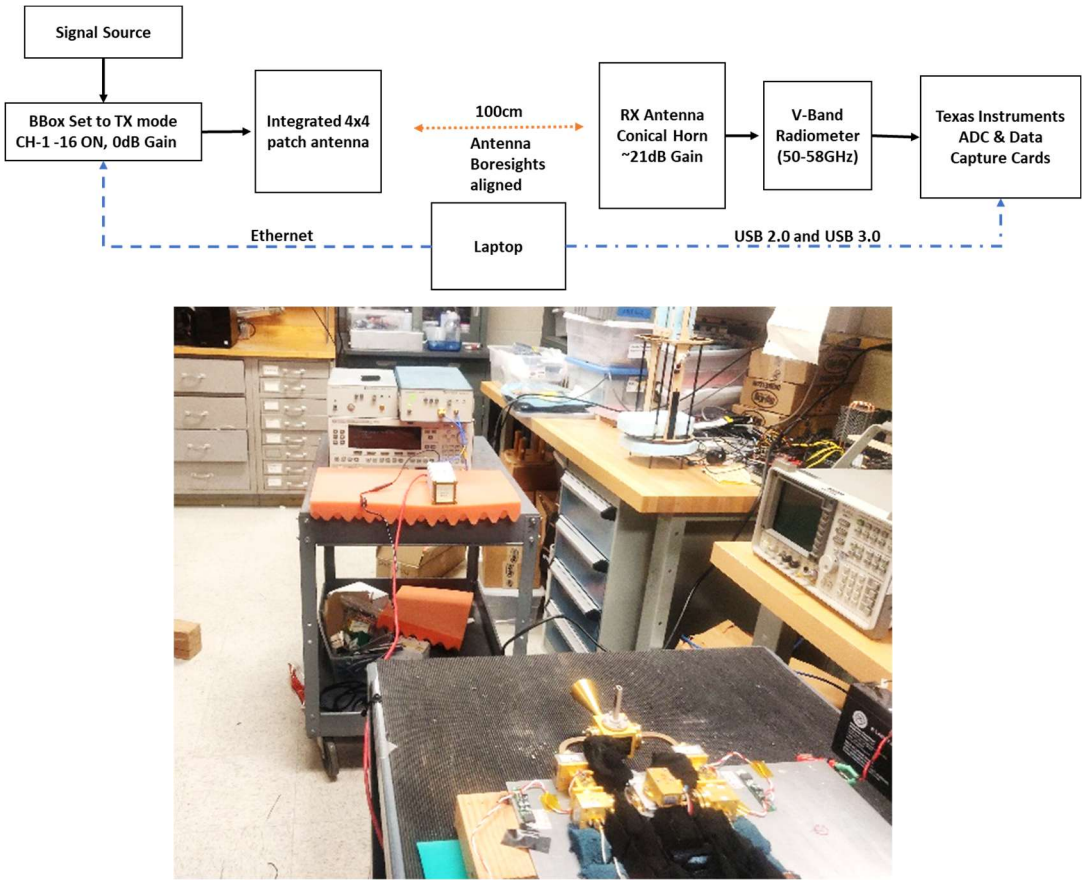

Figure 8.3 Test setup to study V-band second harmonic emissions from BBox-One. Block diagram (above), Laboratory setup (below).

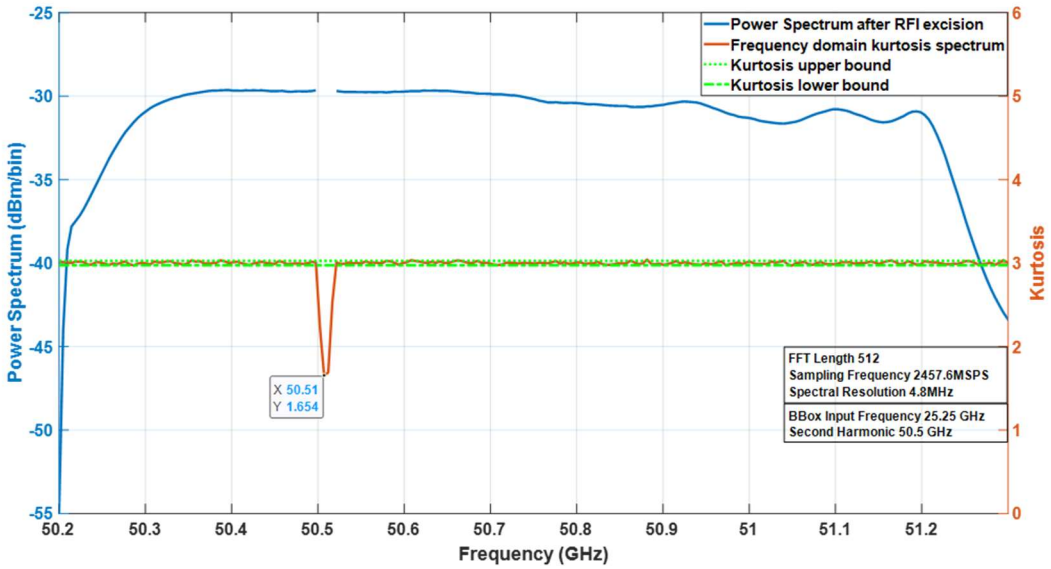

Figure 8.4 RFI due to second harmonic emissions from a 5G beamformer detected and excised using spectral kurtosis.

The radiation pattern of the 4x4 patch antenna array in the second harmonic region will be different from the radiation pattern of the designed frequency range of the antenna. To identify if there was any preferred direction for the second harmonic radiation by the BBox, measurements were taken with the 4x4 patch antenna array pointed in different orientations relative to the radiometer horn antenna. It was observed that the 4x4 patch antenna array response in the second harmonic region was mostly omnidirectional and hence any second harmonic emissions will be radiated in all directions.

An accurate estimate of the interfering power from these devices can be measured using a sensitive spectrometer and is critical to calculate the maximum allowable density of these devices in a unit area. This idea was explored in [35] and for a given brightness temperature retrieval error, the maximum number of these devices in a unit area can be estimated using the density of interferers equation (Figure 8.5).

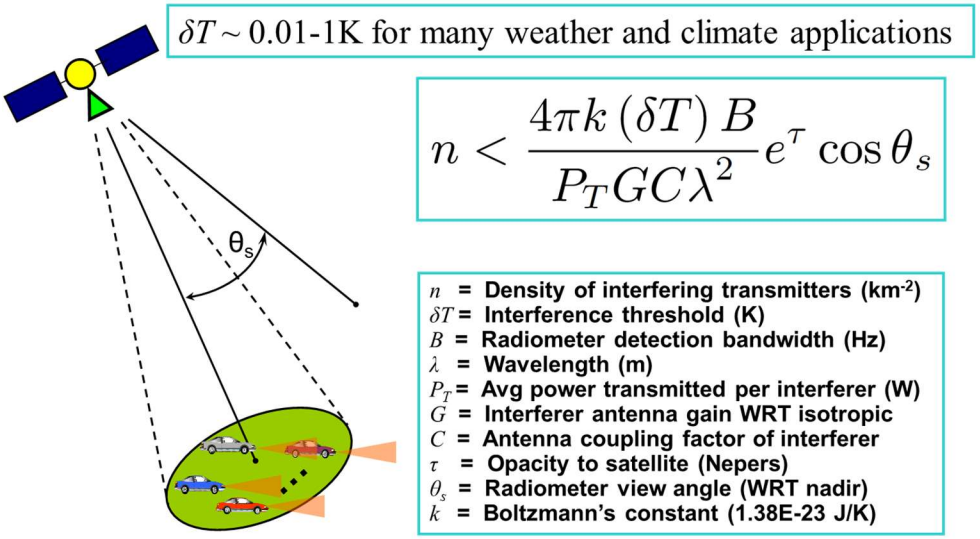

Younis, et al., "Interference from 24-GHz Automotive Radars to Passive Microwave Earth Remote Sensing Satellites," *IEEE Trans. Geosci. Remote Sensing*, 42 (7), 2004.

Figure 8.5 Density of Interferers Equation

Assuming a 5G signal in the n258 band centered at 25.25 GHz and 100MHz bandwidth is transmitted causing second harmonic RFI, the density of interfering transmitters ***n*** (per sq km) emitting isotropic RFI of power P_I in the second harmonic region (50.5GHz, 200MHz) that will cause 10mK error in temperature retrieval is calculated using the density of interferers equation as below.

50.5 GHz 2nd harmonic n258 and n257 emissions

$$\rho < \frac{f^2}{P_I C}\left(4\pi\frac{k}{c^2}\right)(\delta T)\,B\cos\theta_s e^{\alpha h}$$

$$= \frac{(50.5\times10^9)^2}{\left(\left(10^{(-44/10)}\right)\times10^{-3}\right)(1)}\left(\frac{4\pi\,(1.38\times10^{-23})}{(2.998\times10^8)^2}\right)(0.01)\,(2)\,(100\times10^6)\cos(0)\left(10^{(-1/10)}\right)$$

$$= 1.96\times10^{-4}\ \text{m}^{-2} \text{ or } 1.96\times10^{2} \text{ transmitters per square km}$$

$$\langle\Delta_S\rangle = \sqrt{\frac{1}{\rho}} = 71\ \text{m}$$

The number of these devices in a unit area can be increased if the interfering power from each individual unit is lower and vice versa. Table 8 shows the density of devices (km^{-2}) and separation between devices Δs (m) needed between these devices for the 10mK temperature retrieval error in satellite-based temperature measurements.

Interfering Power P_I	Density ρ (km^{-2})	Separation Δs (m)
-44 dBm	1.96e-4	71
-51 dBm	0.001	31.6
-61 dBm	0.01	10
-71 dBm	0.1	3.16

Table 9. Allowed Density of Interferers vs Interfering power for 10mK brightness temperature error in retrieval.

In view of the observations from the second harmonic emissions tests, a 24 GHz HPF and a 31 GHz LPF may be essential for 5G mmwave transmitters to attenuate out-of-band emissions (OOBE) in the 23.6-24.0GHz band and second harmonic emissions in the 50-58GHz band. The studies we have carried out only considered one commercially available 5G beamformer, further studies using different commercial 5G mmwave radio solutions, modulation techniques, and realistic RFI levels is warranted.

CONCLUSION & FUTURE WORK

The first ever 2-path 2SQCC V-band spectrometer instrument based on the Multi-Path Cross Correlation Radiometry (MXCR) technique has been built and tested. The theoretical analysis and mathematical framework to understand the principle of operation of a 2SQCC spectrometer is developed. Brightness temperature retrieval using the 2SQCC MXCR technique is successfully validated by outdoor sky measurements and comparing with the microwave radiative transfer model (MRT). The ability of MCXR concept in retrieving unknown brightness temperatures using predetermined fixed system constants without needing frequent calibration views is demonstrated. The sensitivity of the 2SQCC correlating architecture is compared to that of an ideal single path total radiometer and the results compare within reasonably well. The decreased sensitivity of the 2SQCC architecture compared to the total power radiometer can be compensated through additional integration time available by virtue of needing lesser time for calibration views. Key design considerations in building future instruments based on MXCR concept have been identified. The need for a digital detection scheme for future passive sensing applications in the presence of increased RFI emissions is motivated.

Some of the desirable future work in the 2-path MXCR scheme involves

1. Investigating ways to stabilize and measure noise diode current to better accuracy, thereby minimizing noise diode temperature fluctuations.
2. Real-time processing of the ADC data using FPGAs or ASICs to generate and store accumulated coherency matrix estimates, thereby vastly improving integration time efficiency and sensitivity.
3. A study of the stability of system constants with device temperatures would be beneficial to compensate for thermal drifts, however small they may be.
4. Studying the limits of gain compression and gain fluctuations that can be tolerated by the 2SQCC scheme before the estimation breaks down.

BIBLIOGRAPHY

[1] COP-21 Paris Agreement - United Nations Framework Convention on Climate Change – UN FCCC FCCC/CP/2015/L.9/Rev.1.

[2] Santer, B.D et al, 2017: “Comparing Tropospheric Warming in Climate Models and Satellite Data. J. Climate”, 30, 373–392.

[3] Rosenkranz, P.W., W.J. Blackwell, A.J. Gasiewski, R.V. Leslie, C.A. Mears, J.R. Piepmeier, P.E.Racette, and B.D. Santer, "Designing a Climate-Monitoring Microwave Radiometer," Proceedings of the 2017 USNC URSI Radio Science Meeting, Boulder, CO January4-7, 2017.

[4] IPCC, 2014: Climate Change 2014: Synthesis Report. Contribution of Working Groups I, II and III to the Fifth Assessment Report of the Intergovernmental Panel on Climate Change [Core Writing Team, R.K. Pachauri and L.A. Meyer (eds.)]. IPCC, Geneva, Switzerland, 151 pp.

[5] Gallo,K.P., and Owen,T.W., "Satellite-based adjustments for the urban heat island bias", J. Appl. Meteor, 38(1999), 806–813.

[6] Ferguson,G., and Woodbury,A.D., "Urban heat island in the subsurface", Geophys. Res. Lett., 34 (2007), p. L23713.

[7] Davy, R., and Esau, I.,"Differences in the efficacy of climate forcings explained by variations in atmospheric boundary layer depth", Nature Communications (2016),7:11690.

[8] Doherty, A., Atkinson, N., Bell, W., and Smith, A., "An Assessment of Data from the Advanced Technology Microwave Sounder at the Met Office", Advances in Meteorology, Volume 2015, Article ID 956920.

[9] Smoot, G.; Levin, S. M.; Witebsky, C.; De Amici, G.; Rephaeli, Y. (1987). An Analysis of Recent Measurements of the Temperature of the Cosmic Microwave Background Radiation.

[10] Lu, Q. and W. Bell, 2014: "Characterizing Channel Center Frequencies in AMSU-A and MSU Microwave Sounding Instruments". J. Atmos. Oceanic Technol., 31, 1713–1732.

[11] Gasiewski, A.J., M.A. Hurowitz, B.T. Sanders, D.W. Gallaher, R. Belter, D. Kraft, R. Carter, G. Sasaki, L. Periasamy, K. Zhang, R. Delf, G. Porter, R. McAllister, F. McAllister, and W.L. Hosack, "The Global Environmental Monitoring System (GEMS) Constellation of Passive Microwave Satellites," presented at the 2020 meeting of the American Meteorological Society, Boston, MA January 13-17, 2020.

[12] Powell, D., "New Smallsat Launch Program Will Fly Advanced Microwave Sounder", 99th American Meteorological Society Annual Meeting, Phoenix, AZ, Jan 2019.

[13] Blackwell, W.J., "New Capabilities for All-Weather Microwave Atmospheric Sensing Using CubeSats and Constellations", Small Satellite Conference, AIAA/USU, Aug 2018.

[14] Goldberg et al, 2011: "The Global Space-Based Inter-Calibration System". Bull. Amer. Meteor. Soc., 92, 467–475.

[15] Zou C.Z., Wang W. “Intersatellite Calibration of AMSU-A Observations for Weather and Climate Applications” Journal of Geophysical Research, vol. 116, 2011.

[16] Gasiewski, A.J. "Numerical Sensitivity Analysis of Passive EHF and SMMW Channels to Tropospheric Water Vapor, Clouds, and Precipitation," IEEE Trans. Geosci. Remote Sensing, vol. 30, no. 5, pp. 859 870, September 1992.

[17] U.S. Standard Atmosphere, 1976, U.S. Government Printing Office, Washington, D.C., 1976.

[18] Liebe, H. J., "MPM: an atmospheric millimeter wave propagation model," Int. J. Infrared and Millimeter Waves, 10, 631-650, 1989.

[19] Bhushan, N., J. Li, D. Malladi, R. Gilmore, D. Brenner, A. Damnjanovic, R. Teja Sukhavasi, C. Patel, and S. Geirhofer, "Network Densification: The Dominant Theme for Wireless Evolution into 5G," IEEE Communications Magazine, pp. 82-89, February 2014.

[20] A. Palade, A. M. Voicu, P. Mähönen and L. Simić, "Will Emerging Millimeter-Wave Cellular Networks Cause Harmful Interference to Weather Satellites?," in IEEE Transactions on Cognitive Communications and Networking, vol. 9, no. 6, pp. 1546-1560, Dec. 2023.

[21] A.Venkitasubramony, and A.J.Gasiewski, “A V-band Digital Correlating Spectrometer to Investigate Second Harmonic Emissions from 5G mmwave Transmitters”, NSF Spectrum Week May 2024, Arlington,VA.

[22] "Multipath Cross Correlation Radiometer," Albin J. Gasiewski, PCT serial number PCT/US2023/066012, filed with the USPTO 4/20/2023, Publication number WO2023205734A1.

[23] Gasiewski, A.J., "Multipath Cross-Correlation Radiometry (MXCR)", poster presented at the Fall 2022 SpectrumX Full Team Meeting, October 4-5, University of Virginia, Charlottesville, VA

[24] https://www.minicircuits.com/WebStore/dashboard.html?model=GVA-93%2B

[25] https://www.ti.com/tool/ADC12DJ5200RFEVM

[26] https://www.ti.com/tool/TSW14J57EVM

[27] C.J.Kikkert., "RF Electronics – Design & Simulation" Chapter 8, pp 280-282.

[28] Gasiewski, A.J., ECEN 5254 – Remote Sensing Signals & Systems, Fall 2018, Course Notes

[29] Ulaby,F.T et al, "Microwave Radar and Radiometric Remote Sensing" Chapter-7, page-279.

[30] E. Niiler, "5G networks could throw weather forecasting into chaos," 2019. [Online]. Available: https://www.wired.com/story/5g-networkscould-throw-weather-forecasting-into-chaos/

[31] D. Lubar, D. Kunkee, and L. Cahsin, "Developing a sustainable spectrum approach to deliver 5G services and critical weather forecasts," Center for Space Policy and Strategy, The Aerospace Corporation, 2020

[32] A. Goad et al., "Brokering Spectrum Sharing Using Dynamic Spatial-Spectral Masks," in IEEE Transactions on Electromagnetic Compatibility, vol. 66, no. 4, pp. 1243-1251, Aug. 2024, doi: 10.1109/TEMC.2024.3403510.

[33] S. Misra, R. De Roo and C. Ruf, "Evaluation of the kurtosis algorithm in detecting radio frequency interference from multiple sources," 2010 IEEE International Geoscience and Remote Sensing Symposium, Honolulu, HI, USA, 2010, pp. 2019-2022, doi: 10.1109/IGARSS.2010.5652321.

[34] https://tmytek.com/products/beamformers/bbox

[35] Younis, et al., “Interference from 24-GHz Automotive Radars to Passive Microwave Earth Remote Sensing Satellites," IEEE Trans. Geosci. Remote Sensing, 42 (7), 2004.